

# Numerical Simulations of a Shock-Filament Interaction

J. M. Pittard\* & K. J. A. Goldsmith

*School of Physics and Astronomy, University of Leeds, Woodhouse Lane, Leeds LS2 9JT, UK*

Accepted 11<sup>th</sup> February 2016. Received 11<sup>th</sup> February 2016; in original form 18<sup>th</sup> December 2015

## ABSTRACT

We present 3D hydrodynamic adiabatic simulations of a shock interacting with a dense, elongated cloud. We compare how the nature of the interaction changes with the filament’s length and its orientation to the shock, and with the shock Mach number and the density contrast of the filament. We then examine the differences with respect to 3D spherical-cloud calculations. We find significant differences in the morphology of the interaction when  $M = 10$  and  $\chi = 10^2$ : in many cases 3 parallel rolls are formed, and spread further apart with time, and periodic vortex shedding can occur off the ends of oblique filaments. Sideways-on filaments are accelerated more quickly, and initially lose mass more quickly than spherical clouds due to their greater surface area to volume ratio. However, at late stages they lose mass more slowly, due to the reduced relative speed between the filament and the postshock flow. The acceleration and mixing timescales can vary by a factor of 2 as the filament orientation changes. Oblique filaments can achieve transverse velocities up to 10% of the shock speed. Some aspects of our simulations are compared against experimental and numerical work on rigid cylinders.

**Key words:** hydrodynamics – ISM: clouds – ISM: kinematics and dynamics – shock waves – supernova remnants – turbulence

## 1 INTRODUCTION

In recent years, filaments have gained increasing significance in many areas of astrophysics. *Spitzer* has revealed filamentary structures throughout the galactic disk (e.g., Benjamin et al. 2003; Carey et al. 2009; Churchwell et al. 2009), while *Herschel* images have revealed a complex web of filamentary structures in every interstellar cloud (e.g. André et al. 2010; Men’shchikov et al. 2010; Molinari et al. 2010; Henning et al. 2010; Motte et al. 2010), whether or not stars have formed in them. Goodman et al. (2014) argue that filamentary molecular structures can extend many hundreds of parsecs in length, and make up the “bones” of the Milky Way. The filaments are thought to form out of compressed gas due to converging flows, which are driven by interstellar turbulence, by large scale spiral arms, or by gravitational disk instabilities. In support of these observations, simulations of molecular clouds consistently show the formation of filamentary structure (e.g., Klessen & Burkert 2000; Ballesteros-Paredes & Mac Low 2002; Bate & Bonnell 2005; Padoan et al. 2006; Vázquez-Semadeni 2006; Heitsch & Hartmann 2008; Federrath et al. 2010; Krumholz et al. 2011; Glover & Clark 2012; Bonnell et al. 2013; Hennebelle 2013; Gómez &

Vázquez-Semadeni 2014; Smith et al. 2014; Kirk et al. 2015; Moeckel & Burkert 2015).

Some molecular cloud filaments are likely to be transitory objects, but others collapse further under gravity and fragment into star-forming cores. The resulting stars help to disperse the remaining parts of the filament through their ionizing radiation and winds/outflows. However, the efficiency of this process remains contentious: Dale & Bonnell (2011) find that the ionizing flux from massive clusters forming at the base of strong filamentary accretion flows has little effect on the filaments, while Colín et al. (2013) find that massive stars are able to completely evacuate dense gas to 10 pc distances. Filaments located near regions of massive star formation can also be strongly affected by high speed shocks and winds. For example, the B59 filament in the Pipe Nebula is clearly being shaped by a wind from the nearby Sco OB2 association (Peretto et al. 2012). Similarly, the winds and radiation from the OB stars in the Cyg OB2 and Cyg OB9 associations appear to be affecting the molecular clouds of the Cyg X complex (Schneider et al. 2006), while Wilson et al. (2005) suggest that stellar wind driven compression is consistent with the kinematics and structure of the CO gas in Orion A and Orion B. Winds may also play a part in disrupting molecular clouds, such as the Rosette nebula (Bruhweiler et al. 2010). Dent et al. (2009) note that the near constant velocity gradient over an extended clump in the Rosette nebula is difficult to explain with radiatively

\* E-mail: jmp@ast.leeds.ac.uk (JMP)

driven models of clump acceleration. The lifetime of filamentary features in a molecular clump exposed to stellar winds and supernova explosions was investigated by Rogers & Pittard (2013).

Filaments are also observed in young protoclusters (e.g., Vig et al. 2007), in galactic outflows (e.g., Shopbell & Bland-Hawthorn 1998; Ohyaama et al. 2002; Martin et al. 2002; Strickland et al. 2004; Hoopes et al. 2005; Veilleux et al. 2005; Engelbracht et al. 2006; Westmoquette et al. 2011; Heeson et al. 2011; Bolatto et al. 2013) and in clusters of galaxies (e.g., Conselice et al. 2001; Crawford et al. 2005; Forman et al. 2007; McDonald et al. 2010; Canning et al. 2011) and are reproduced in simulations of these sources (e.g., Rodríguez-González et al. 2008; Strickland & Stevens 2000; Cooper et al. 2008; Fujita et al. 2009; Gaspari et al. 2012). The emission from galactic winds is dominated by shock excitation (e.g., Veilleux & Rupke 2002; Sharp & Bland-Hawthorn 2010; Rich et al. 2010), indicating that these filamentary regions are inundated by shocks.

As a first step towards understanding the effect of mechanical feedback on a filament, we perform idealized numerical simulations of an adiabatic shock striking a non-magnetized filament. This represents the most basic setup for a shock-filament interaction, and is appropriate for our initial study. The assumption of adiabaticity implies that our work is relevant in the small cloud and/or low density limit (see, e.g., Klein et al. 1994). It requires that the evolutionary timescale of the cloud is shorter than the cooling timescale. In the interstellar medium (ISM), diffuse filaments in an ionized or atomic phase may satisfy this criteria. In future work we will examine the effects of winds, magnetic fields and radiative cooling. In Sec. 2 we introduce the shock-filament problem and review the current literature. In Sec. 3 we describe the numerical methods, the initial and boundary conditions, and the time-scales and statistics used in our study. In Sec. 4 we present our results and in Sec. 5 we summarize our conclusions. A resolution test is presented in an Appendix.

## 2 PROBLEM DEFINITION

An adiabatic shock striking a non-magnetized filament represents the most basic idealized scenario of a shock-filament interaction. The interaction depends on five parameters: 1) the Mach number of the shock,  $M$ ; 2) the density contrast of the filament,  $\chi$ ; 3) the filament aspect ratio; 4) the orientation of the filament; 5) the ratio of specific heats,  $\gamma$ . As no physical scales are imposed on the problem, our simulations can be scaled to any desired length- or time-scales. In the strong shock limit ( $M \gg 1$ ), we can expect Mach-scaling to also hold (e.g., Klein et al. 1994), so our high Mach number calculations will be representative of any other high Mach number simulation.

Our idealized filament is assumed to have a cylindrical centre, of length  $lr_c$ , where  $r_c$  is the filament radius, which is capped by a hemisphere at each end (see, e.g., Fig. 3). We choose this definition so that spherical clouds have  $l = 0$ . The total length of the filament is  $(l + 2)r_c$ , and the ratio of the lengths of its major and minor axes is  $(l + 2)/2$ . The filament's orientation is specified by the angle  $\theta$ , which is the angle between its major-axis and the shock *surface*. Our

setup is clearly idealized, not least because observations of actual filaments in molecular clouds show a great deal of sub-structure (e.g., Hacar et al. 2013; Fernández-López et al. 2014; Henshaw et al. 2014), and may be composed of multiple strands of gas.

Nevertheless, this description is adequate for our purposes and allows us to investigate how the interaction changes as  $M$ ,  $\chi$ ,  $l$ , and  $\theta$  are varied. The filament is assumed to have soft edges over about 10 per cent of its radius (we adopt  $p_1 = 10$  in keeping with our earlier work, cf. Pittard et al. 2009, 2010; Pittard & Parkin 2016). Filaments in molecular clouds with a Plummer-like density profile are like soft-edged clouds and we can expect that instabilities will take relatively longer to develop (see Nakamura et al. 2006). The filament is also in pressure equilibrium with its surroundings which have a mass density of  $\rho_{\text{amb}}$ .

### 2.1 Previous numerical studies of shock-cloud interactions

The first numerical studies of a planar adiabatic shock striking a single isolated spherical cloud were published in the 1970s. The nature of the interaction changes with the specific values of  $M$  and  $\chi$ , and the cloud's density profile, but in all cases the cloud is initially compressed and then re-expands. Vorticity is deposited at the surface of the cloud, and the cloud is subject to numerous dynamical instabilities, including Kelvin-Helmholtz (KH), Rayleigh-Taylor (RT) and Richtmyer-Meshkov (RM) (e.g., Klein, McKee & Colella 1994). The vorticity deposition and growth of KH instabilities is strongest when the cloud has sharp edges. The interaction is more gentle at lower Mach numbers and for clouds with soft edges (e.g., Nakamura et al. 2006; Pittard et al. 2010; Pittard & Parkin 2016). The cloud is more rigid, and is better able to resist the passage of the shock, as  $\chi$  increases (see, e.g., Pittard et al. 2010). For all but weak shocks, the interaction is characterized by a series of shocks and rarefaction waves moving through the cloud which cause the cloud to reverberate - at some moments in time the cloud is pancaked, while at other moments the cloud becomes hollow and “voided”. Shocks leaving the cloud introduce reflected rarefaction waves into the cloud, and shocks into the external medium. Rarefaction waves within the cloud which reach the cloud boundary introduce a transmitted rarefaction wave into the external medium and a reflected shock which moves back into the cloud.

For relatively sharp-edged clouds, the cloud lifetime,  $t_{\text{life}}$ , defined as when material from the core of the cloud is well mixed with the ambient material, is  $\sim 6 t_{\text{KHD}}$ , where  $t_{\text{KHD}}$  is the growth-timescale for the most disruptive, long-wavelength, KH instabilities (Pittard et al. 2010; Pittard & Parkin 2016). At high Mach numbers and for  $\gamma = 5/3$ , this is equivalent to  $t_{\text{life}} \sim 8 t_{\text{cc}}$ . In 3D simulations, non-axisymmetric instabilities develop (Stone & Norman 1992; Klein et al. 2003; Niederhaus et al. 2008), but for sharp-edged and reasonably sharp-edged clouds these do not significantly affect either the cloud lifetime or its acceleration (Pittard & Parkin 2016). Klein et al. (2003) argued that the break-up of the vortex ring in 3D experiments and simulations led to significant differences in the hollowing or “voiding” of the cloud compared to 2D simulations. However, Pittard & Parkin (2016) showed that 2D axisymmetric and fully

3D simulations evolve almost identically until the late stages of the interaction, and put this contradiction down to the different numerical codes and initial conditions used by Klein et al. (2003).

While the hydrodynamical nature of the interaction of a shock with a spherical cloud is now well understood, very little work exists in the current literature on how the interaction changes when the cloud is not spherical. Klein et al. (1994) were amongst the first to look into this when they investigated the interaction of a shock with a cloud with an aspect ratio of 3:1 (see their Sec 9.1). Their calculation was in 2D axisymmetry with the long-axis of the cloud aligned with the direction of propagation of the shock (so the “filament” was hit from one end). They introduced a modified cloud crushing timescale ( $t'_{cc}$ , their Eq. 9.2) and found reasonably good agreement with the spherical case when comparing as a function of  $t'_{cc}$ . Therefore, Klein et al. (1994) noted that their main conclusions were unaffected by modest changes in the initial shape of the cloud.

Xu & Stone (1995) conducted some of the first 3D shock-cloud simulations in order to investigate how the interaction depends on the shape of the cloud. Their use of 3D allowed arbitrary orientations of the cloud relative to the shock, thus avoiding the restrictions in Klein et al. (1994)’s work. They instead noted that the nature of the interaction *is* quite different for spherical and prolate clouds: an aligned prolate cloud does not form a vortex ring, and accelerates faster than a spherical cloud, whereas an inclined prolate cloud is “spun around” and instabilities develop differently. They further found that the mixing rate of a prolate cloud is much faster than a spherical cloud of the same mass as a result of the higher surface-to-volume ratio of the cloud. In both of their calculations an axial ratio of 2:1 was adopted.

To our knowledge, there exists no other dedicated numerical study of shocks striking prolate or filamentary clouds. The current work therefore extends the investigations of Klein et al. (1994) and Xu & Stone (1995) to interactions where the aspect ratio of the cloud and its density contrast are greater. Our work builds on recent spherical-cloud simulations where the dependence of the interaction with a shock was explored for a variety of density contrasts and shock Mach numbers (Pittard et al. 2010; Pittard & Parkin 2016).

### 3 THE NUMERICAL SETUP

The calculations were performed on a 3D XYZ cartesian grid using the MG Eulerian adaptive mesh refinement (AMR) hydrodynamic code (Falle 1991). The normal Eulerian equations are solved for conservation of mass, momentum and energy:

$$\frac{\partial \rho}{\partial t} + \nabla \cdot (\rho \mathbf{u}) = 0, \quad (1)$$

$$\frac{\partial \rho \mathbf{u}}{\partial t} + \nabla \cdot (\rho \mathbf{u} \mathbf{u}) + \nabla P = 0, \quad (2)$$

$$\frac{\partial E}{\partial t} + \nabla \cdot [(E + P)\mathbf{u}] = 0, \quad (3)$$

where  $\rho$  is the mass density,  $\mathbf{u}$  is the velocity,

$$E = \frac{P}{\gamma - 1} + \frac{1}{2} \rho \mathbf{u}^2 \quad (4)$$

is the total energy density, and  $P$  is the thermal pressure.

MG uses piece-wise linear cell interpolation and solves the Riemann problem at cell interfaces to obtain the conserved fluxes for the time update. A linear solver is used for most cases, with the code switching to an exact solver when there is a large difference between the two states. The flux update occurs for all directions simultaneously. The time integration proceeds first with a half time-step to obtain fluxes at this point. The conserved variables are then updated over the full time-step. The code is thus 2<sup>nd</sup>-order accurate in space and time.

The two coarsest levels ( $G^0$  and  $G^1$ ) cover the whole computational domain, and finer cells are added or removed as needed. Steep gradients in the fluid variables, such as at shocks or contact discontinuities, cause the mesh to be more refined than in more uniform regions. Each level is generated from its predecessor by doubling the number of computational grid cells in each spatial direction. This technique enables the generation of fine grids in regions of high spatial and temporal variation, and conversely, relatively coarse grids where the flow field is numerically smooth. Values for newly created cells are obtained by linear interpolation from the coarser level. To maintain accuracy, the solution in finer grid cells overwrites that in coarser cells, and flux corrections are applied at coarse-fine boundaries. Double refinements are not allowed.

Refinement is performed on a cell-by-cell basis and is controlled by the difference in the solutions on the coarser grids. In this work only the difference in density is compared, and cells are marked for refinement if  $|\rho_f - \rho_{ic}| > 0.01 \rho_f$ , where  $\rho_f$  is the density in the fine cell and  $\rho_{ic}$  is the interpolated density from the coarser cell, *before* the solution in the coarse cell has been overwritten by that in the finer cells. In this way the refinement algorithm really is comparing an error. In all of our calculations the  $G^0$  grid has a cell width of  $2r_c$ , so that calculations with 32 cells across the filament semi-minor axis on the finest grid (henceforth  $R_{32}$ ) use 7 grid levels in total ( $G^0$  to  $G^6$ ).

In this work we conduct a purely hydrodynamic study, and ignore the effects of magnetic fields, thermal conduction, cooling and self-gravity. All calculations were performed for an ideal gas with  $\gamma = 5/3$  and are adiabatic. Our calculations are thus scale-free and can be easily converted to any desired physical scales.

An advected scalar is used to distinguish between cloud and ambient material, and thus to track the ablation and mixing of the cloud, and the cloud’s acceleration by the passage of the shock and subsequent exposure to the post-shock flow. The filament is initially centered at the grid origin ( $X, Y, Z$ ) = (0, 0, 0) while the shock is located at  $X = -10$ . The grid has zero gradient conditions on each boundary and is set large enough so that the filament is well-dispersed and mixed into the post-shock flow before the shock reaches the downstream boundary. The grid extent is dependent on  $M$ ,  $\chi$ , and the filament orientation and is noted in Table 1. Note that we do not impose any symmetry constraints on the interaction, unlike the earlier work of Xu & Stone (1995). We define motion in the direction of shock propagation as “ax-

**Table 1.** The grid extent as a function of  $M$  and  $\chi$ . The unit of length is the filament radius,  $r_c$ . Note that simulations *m10c2l8o30*, *m10c2l8o60* and *m10c2l8o85* actually had  $Y$  and  $Z$  extents of  $-16 < Y < 16$ , and  $-33 < Z < 15$ ,  $-25 < Z < 15$ , and  $-20 < Z < 20$ , respectively. In all cases the filament is centered at the grid origin, while the shock is initialized at  $X = -10$  and propagates in the  $+X$  direction.

| $M$ | $\chi$     | $X$              | $Y$            | $Z$            |
|-----|------------|------------------|----------------|----------------|
| 10  | 10         | $-20 < X < 160$  | $-24 < Y < 24$ | $-16 < Z < 16$ |
| 10  | $10^2$     | $-20 < X < 160$  | $-24 < Y < 24$ | $-16 < Z < 16$ |
| 10  | $10^3$     | $-20 < X < 460$  | $-24 < Y < 24$ | $-16 < Z < 16$ |
| 3   | $10, 10^2$ | $-20 < X < 160$  | $-24 < Y < 24$ | $-16 < Z < 16$ |
| 1.5 | $10, 10^2$ | $-120 < X < 160$ | $-24 < Y < 24$ | $-24 < Z < 24$ |

ial” (the shock propagates along the  $X$ -axis), while motion perpendicular to this (in the  $Y$  and  $Z$  directions) is termed “radial” or “transverse”.

The filament evolution is studied through various integrated quantities (see Klein et al. 1994; Nakamura et al. 2006; Pittard et al. 2009; Pittard & Parkin 2016). Averaged (mass-weighted) quantities  $\langle f \rangle$ , are constructed by

$$\langle f \rangle = \frac{1}{m_\beta} \int_{\kappa \geq \beta} \kappa \rho f dV, \quad (5)$$

where the mass identified as being part of the filament is

$$m_\beta = \int_{\kappa \geq \beta} \kappa \rho dV. \quad (6)$$

$\kappa$  is an advected scalar, which has an initial value of  $\rho/(\chi \rho_{\text{amb}})$  for cells within a distance of  $r_c$  from the “edge” of the filament, and a value of zero at greater distances. Hence,  $\kappa = 1$  in the centre of the filament, and declines outwards. The above integrations are performed only over cells in which  $\kappa$  is at least as great as the threshold value,  $\beta$ . Setting  $\beta = 0.5$  probes only the densest parts of the filament and its fragments (hereafter identified with the subscript “core”), while setting  $\beta = 2/\chi$  probes the whole filament including its low density envelope, and regions where only a small percentage of filament material is mixed into the ambient medium (identified with the subscript “cloud”).

The mean density is defined as

$$\langle \rho \rangle = \frac{m_\beta}{V_\beta}, \quad (7)$$

where  $V_\beta$  is the volume of the region with  $\kappa \geq \beta$ . We also monitor the mass-weighted mean velocity of the filament in each direction -  $\langle v_x \rangle$ ,  $\langle v_y \rangle$ , and  $\langle v_z \rangle$  - and the velocity dispersions in each of the 3 directions, which are defined as

$$\delta v_x = (\langle v_x^2 \rangle - \langle v_x \rangle^2)^{1/2}, \quad (8)$$

$$\delta v_y = (\langle v_y^2 \rangle - \langle v_y \rangle^2)^{1/2}, \quad (9)$$

$$\delta v_z = (\langle v_z^2 \rangle - \langle v_z \rangle^2)^{1/2}. \quad (10)$$

The characteristic time for a spherical cloud to be crushed by the shocks driven into it is the “cloud crushing” time,  $t_{\text{cc}} = \chi^{1/2} r_c / v_b$ , where  $v_b$  is the velocity of the shock in the intercloud (ambient) medium. Klein et al. (1994) also introduced a “modified cloud crushing time” for cylinder-

shaped clouds,

$$t'_{\text{cc}} \equiv \frac{(\chi a_0 c_0)^{1/2}}{v_b}, \quad (11)$$

where  $a_0$  and  $c_0$  are the initial radius of the cloud in the radial and axial directions, respectively. Xu & Stone (1995) instead adopt

$$t_{\text{cs}} \equiv \frac{r_s \chi^{1/2}}{v_b}, \quad (12)$$

where  $r_s$  is the radius of a spherical cloud of equivalent mass. We will determine which of  $t_{\text{cc}}$ ,  $t'_{\text{cc}}$  and  $t_{\text{cs}}$  gives the tightest comparison between models.

Several other timescales are obtained from the simulations. The time for the average velocity of the cloud relative to that of the postshock ambient flow to decrease by a factor of  $e$  (i.e. when the average cloud velocity  $\langle v \rangle_{\text{cloud}} = (1 - 1/e) v_{\text{ps}}$ , where  $v_{\text{ps}}$  is the speed of the postshock ambient medium as measured in the frame of the preshock ambient gas) is defined as the “drag time”,  $t_{\text{drag}}$  (see Klein et al. 1994, who also provide analytical expressions for the time dependence of the mean cloud velocity for both spherical and cylinder-shaped clouds)<sup>1</sup>. The “mixing time”,  $t_{\text{mix}}$ , is defined as the time when the mass of the core of the filament,  $m_{\text{core}}$ , reaches half its initial value. Similarly, we define the “lifetime”,  $t_{\text{life}}$ , as the time when  $m_{\text{core}}$  reaches 1% of its initial value. The zero-point of all time measurements occurs when the intercloud shock is level with the centre of the filament.

## 4 RESULTS

As with any hydrodynamical study, it is important to investigate the spatial resolution which is necessary to resolve key features in the flow (e.g., the bow shock, the turbulent boundary layer, etc.). Previous 2D studies have indicated that about 100 cells per cloud radius is necessary (e.g., Klein et al. 1994; Nakamura et al. 2006), which is the point at which the turbulent boundary layer becomes resolved (Pittard et al. 2009). Use of a  $k-\epsilon$  subgrid turbulence model negates the need to resolve this layer (it is instead handled by the subgrid physics) and can reduce the resolution requirement to about 30 cells per cloud radius in 2D simulations (Pittard et al. 2009). “Inviscid” and  $k-\epsilon$  2D axisymmetric simulations can behave significantly differently, which is likely due to the different behaviour of vortices in 2D and 3D. The most detailed resolution study of 3D shock-cloud interactions to date has been presented by Pittard & Parkin (2016), where it is seen that “inviscid” and  $k-\epsilon$  simulations are in perfect agreement until the turbulent boundary layer starts to become resolved. Resolutions of 32-64 cells per cloud radius are necessary to resolve the main flow features and for some properties to show signs of convergence.

In Appendix A we carry out a similar study for shock-filament interactions. We find that a resolution of  $R_{32}$  across the semi-minor axis is the minimum necessary, and adopt this value for the rest of this work. Most of our calculations are

<sup>1</sup> Note that the definition of  $t_{\text{drag}}$  in Pittard et al. (2009, 2010) is for the relative cloud velocity to decrease by a factor of  $1/e$ , which is obtained when  $\langle v \rangle_{\text{cloud}} = v_{\text{ps}}/e$ . This definition of  $t_{\text{drag}}$  gives smaller values than the definition of Klein et al. (1994).



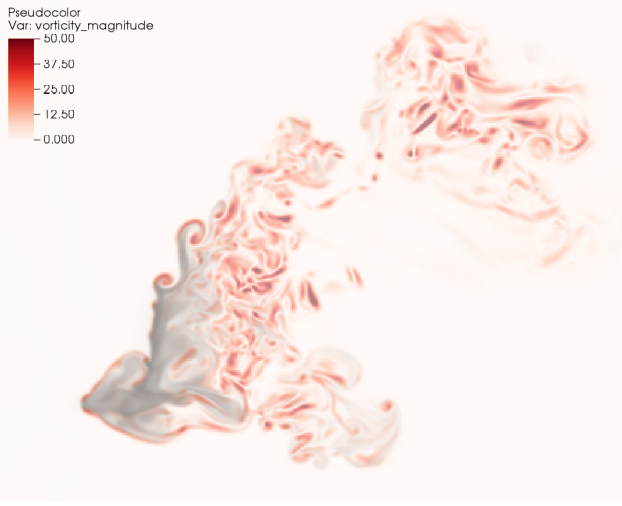


**Figure 8.** Periodic vortex shedding in simulation *m10c2l8s030*. The greyscale shows the logarithm of the mass density in the  $XZ$  plane at  $Y = 0$  and  $t = 2.98 t_{cs}$ . The redscale indicates the vorticity magnitude. The  $(X, Z)$  extent of the frame (in units of  $r_c$ ) is  $(5 - 30, \pm 10)$ .

for  $M = 10$  and  $\chi = 10^2$  and the length and orientation of the filament are varied. We consider values of  $l$  up to 8. We adopt a naming convention such that our reference simulation is *m10c2l8s* - here the *m10* indicates the shock Mach number, the *c2* indicates a density contrast of  $10^2$ , the *l8* indicates that  $l = 8$ , and the *s* indicates that the filament is sideways on. Where the filament has an oblique orientation to the shock, we replace “*s*” with “*oθ*”, where  $\theta$  is the angle between the shock *surface* and the long axis of the filament (thus the “sideways-on” simulations could equally as well have been designated as “*o0*”). Towards the end of this section we also discuss results from simulations with different Mach numbers and density contrasts. Table 2 summarizes the simulations performed and some of their key parameters. After examining the filament morphology during the interaction, we present the evolution of some key global quantities and then study the mixing and drag time of the filament.

#### 4.1 Filament morphology and turbulence

##### 4.1.1 The interaction of an $M = 10$ shock and a $\chi = 10^2$ sideways oriented ( $\theta = 0^\circ$ ) filament

We begin by examining the morphology of the interaction for our reference simulation, which has  $M = 10$ ,  $\chi = 10^2$ ,  $l = 8$ , and has the filament oriented sideways to the shock (simulation *m10c2l8s*). Volumetric renderings of the density of *filament* material are shown as a function of time in Figs. 1 and 2. Because of this focus, in these and similar figures, the bowshock and other features in the ambient material are not visible. The snapshots shown in these figures are at identical times. We also show the mass density on 2 orthogonal slices through the simulation, as a function of time, in Fig. 3. This figure shows the bowshock and other features in the ambient material which are not visible in Figs. 1 and 2, and also adds 2 more snapshots. Note that Fig. 3 focusses on slightly earlier times. The first panel shows the initial orientation

of the filament (the shock is located at the left edge of the image). Shocks are easier to identify in Fig. 3, while the 3D morphology is better conveyed in Figs. 1 and 2. Together, Figs. 1-3 reveal the nature of the interaction.

Figs. 1-3 show the shock striking the filament from its side. A transmitted shock is sent through the filament, while the external part of the shock diffracts around the filament, remaining nearly normal to the filament surface as it sweeps towards the downstream side. At  $t = 0.01 t_{cs}$  the external shock has just passed the centre of the filament. The bowshock upstream of the filament is visible, and the transmitted shock can be seen entering the filament. At  $t = 0.18 t_{cs}$  the transmitted shock is nearly half-way through the filament. Meanwhile the external shock has completely swept over the filament. There is a region of high pressure immediately downstream of the filament caused by the focusing of the diffracted external shock and its subsequent convergence on the  $Z = 0$  plane (this is best seen in the lower part of the panel which shows the  $XZ$  plane). This high pressure region starts to drive a shock into the back of the filament, towards its front surface. Also visible are the diffracted shocks which move from the ends of the filament towards the  $Y = 0$  plane. These shocks are not seen in spherical cloud interactions. Finally we note that some material is already being ablated from the filament surface, from its ends (see the  $XY$  plane) and along its length (see the  $XZ$  plane).

At  $t = 0.53 t_{cs}$  we see the filament at almost its most compressed. The transmitted shock has just left the back of the filament at this point, accelerating into the downstream ambient gas (it is visible as the planar feature located just downstream of the filament in Fig. 3). As a consequence of the transmitted shock reaching the back of the filament, a rarefaction wave is launched and moves back upstream through the filament. At this moment we see that the tips of the filament curve upstream. The expansion of the filament due to the rarefaction waves passing through it is readily visible at  $t = 0.88 t_{cs}$ . The back of the filament has a “fluted” structure at this point (visible in the  $XZ$ -plane in Fig. 3). A strong tail-shock is also visible some distance downstream from the back of the filament.

At  $t = 1.23 t_{cs}$  the RT instability has given the filament a 3-pronged structure along its length, while additional RT fingers are present at the filament ends. KH instabilities can be seen in the  $Z = 0$  plane along the front of the filament at  $t = 1.58 t_{cs}$ . By this time, the secondary shocks and rarefaction waves which are moving through the filament cause it to “reverberate”. Vorticity deposited on the surface of the filament drives the growth of KH instabilities which rip material from the filament and create a complex tail. It is material in the tail which is visible above and below the filament in the third panel of Fig. 2.

The filament enters the late stages of its destruction by  $t = 2.28 t_{cs}$ , having been fragmented into 3 parallel “rolls” by the RT instability. The central roll displayed in the  $Z = 0$   $XY$ -plane shows numerous small-scale features and signs of instabilities, and is beginning to bend into an arc-like structure as the ends of the rolls are pushed faster downstream by the external flow. RM fingers are visible on the front surface of the filament in Fig. 1. The rolls are driven away from each other as the postshock gas tries to flow between them. The wake behind the filament reaches a turbulent-like state, and

**Table 2.** A summary of the simulations investigated in this work and some key results.  $M$  is the shock Mach number,  $\chi$  is the density contrast of the filament with respect to the ambient medium, and  $l$  defines the length of the filament. The filament is either oriented at an angle  $\theta$  between its major-axis and the shock *surface*, or is sideways-on to the shock ( $\theta = 0^\circ$ ).  $t'_{cc}$  is the modified cloud-crushing timescale of Klein et al. (1994) (their Eq. 9.2) while  $t_{cs}$  is the cloud-crushing timescale for a spherical cloud of equivalent mass introduced by Xu & Stone (1995). Key timescales and filament properties are also noted. Times in parentheses in columns 8 and 9 are in units of  $t_{cs}$  instead of  $t_{cc}$ . Results in parentheses in the final three columns indicate values computed for the “core”, while those without are computed for the more extended “cloud”.  $\langle \rho \rangle / \rho_{\max}$ ,  $\langle v_x \rangle / v_b$ , and  $\langle x \rangle$  are evaluated at  $t = t_{\text{mix}}$ .

| Name       | $M$ | $\chi$          | $l$ | Orientation | $t'_{cc}/t_{cc}$ | $t_{cs}/t_{cc}$ | $t_{\text{drag}}/t_{cc/cs}$ | $t_{\text{mix}}/t_{cc/cs}$ | $t_{\text{mix}}/t_{\text{drag}}$ | $\langle \rho \rangle / \rho_{\max}$ | $\langle v_x \rangle / v_b$ | $\langle x \rangle$ |
|------------|-----|-----------------|-----|-------------|------------------|-----------------|-----------------------------|----------------------------|----------------------------------|--------------------------------------|-----------------------------|---------------------|
| m10c2l8s   | 10  | 100             | 8   | sideways    | 2.236            | 1.943           | 4.69 (2.42)                 | 7.06 (3.64)                | 2.54                             | 0.016 (0.092)                        | 0.589 (0.554)               | (21.2)              |
| m10c2l4s   | 10  | 100             | 4   | sideways    | 1.732            | 1.587           | 4.45 (2.80)                 | 6.32 (3.92)                | 2.26                             | 0.017 (0.086)                        | 0.575 (0.543)               | (17.6)              |
| m10c2l2s   | 10  | 100             | 2   | sideways    | 1.414            | 1.357           | 4.25 (3.13)                 | 5.76 (4.20)                | 2.05                             | 0.017 (0.087)                        | 0.568 (0.524)               | (14.8)              |
| m10c2l8o85 | 10  | 100             | 8   | 85°         | 2.236            | 1.943           | 7.82 (4.03)                 | 8.40 (4.33)                | 1.60                             | 0.014 (0.087)                        | 0.514 (0.430)               | (11.9)              |
| m10c2l8o60 | 10  | 100             | 8   | 60°         | 2.236            | 1.943           | 8.92 (4.59)                 | 9.70 (5.00)                | 1.62                             | 0.013 (0.045)                        | 0.506 (0.401)               | (14.9)              |
| m10c2l8o30 | 10  | 100             | 8   | 30°         | 2.236            | 1.943           | 6.00 (3.09)                 | 8.32 (4.28)                | 2.31                             | 0.014 (0.071)                        | 0.579 (0.551)               | (23.4)              |
| m10c3l8s   | 10  | 10 <sup>3</sup> | 8   | sideways    | 2.236            | 1.943           | 6.05 (3.12)                 | 6.46 (3.33)                | 1.49                             | 0.0011 (0.011)                       | 0.491 (0.395)               | (28.6)              |
| m10c2l4o30 | 10  | 100             | 4   | 30°         | 1.732            | 1.587           | 6.07 (3.82)                 | 7.78 (4.83)                | 2.19                             | 0.013 (0.070)                        | 0.561 (0.510)               | (19.9)              |
| m10c2l2o30 | 10  | 100             | 2   | 30°         | 1.414            | 1.357           | 5.24 (3.86)                 | 6.54 (4.77)                | 1.91                             | 0.014 (0.065)                        | 0.585 (0.549)               | (15.5)              |
| m1.5c1l8s  | 1.5 | 10              | 8   | sideways    | 2.236            | 1.943           | 6.47 (3.33)                 | 25.4 (13.1)                | 10.8                             | 0.129 (0.24)                         | 0.317 (0.335)               | (22.6)              |
| m3c1l8s    | 3   | 10              | 8   | sideways    | 2.236            | 1.943           | 2.94 (1.51)                 | 12.8 (6.57)                | 14.3                             | 0.202 (0.39)                         | 0.526 (0.544)               | (18.8)              |
| m10c1l8s   | 10  | 10              | 8   | sideways    | 2.236            | 1.943           | 2.13 (1.10)                 | 10.1 (5.22)                | 14.7                             | 0.250 (0.49)                         | 0.603 (0.605)               | (17.6)              |
| m1.5c2l8s  | 1.5 | 100             | 8   | sideways    | 2.236            | 1.943           | 16.1 (8.30)                 | 16.4 (8.45)                | 2.47                             | 0.0096 (0.043)                       | 0.266 (0.241)               | (21.1)              |
| m3c2l8s    | 3   | 100             | 8   | sideways    | 2.236            | 1.943           | 6.34 (3.27)                 | 8.21 (4.23)                | 2.29                             | 0.014 (0.076)                        | 0.492 (0.448)               | (19.4)              |

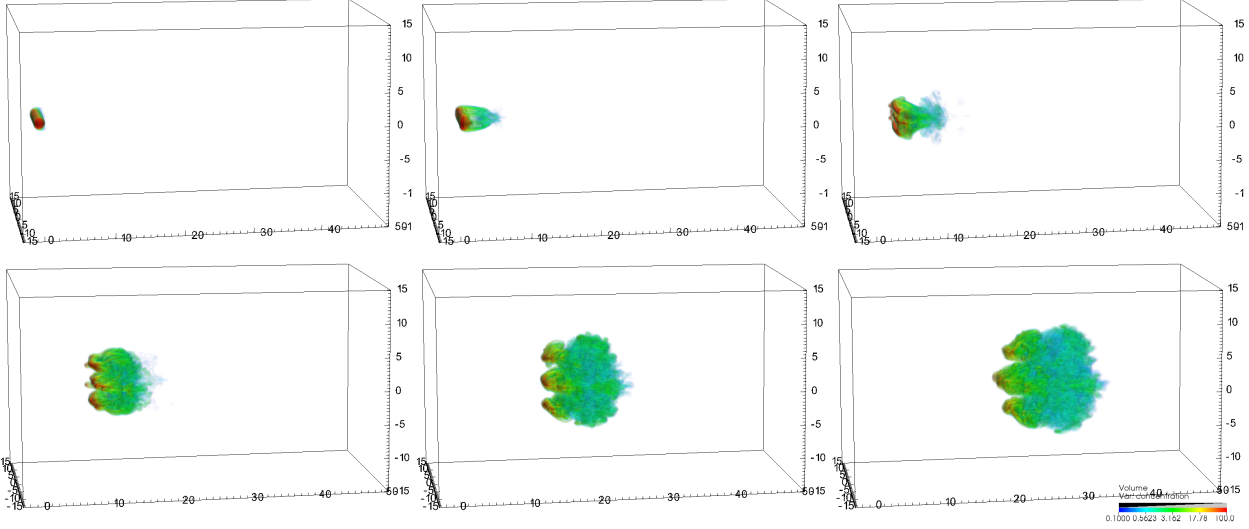


**Figure 1.** A 3D volumetric rendering of the time evolution of simulation *m10c2l8s*. From left to right and top to bottom the times are  $t = 0.18, 0.88, 1.58, 2.28, 2.98$  and  $3.68 t_{cs}$  ( $t = 0$  is defined as the time when the intercloud shock is level with the centre of the filament). The colour indicates the density of the filament material, normalized by the ambient density (i.e. the initial filament density is 100). Since the ambient material is not shown the bowshock upstream of the filament is not visible. The actual grid extends much further than the bounding box shown.  $t_{\text{drag}} = 2.42 t_{cs}$  and  $t_{\text{mix}} = 3.64 t_{cs}$ .

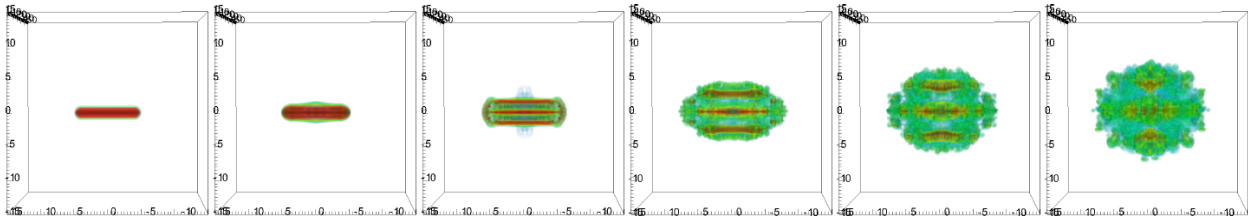


**Figure 2.** As Fig. 1 but viewing from the front. It is clear that the filament preferentially expands along its minor axis, parallel to the shock front.

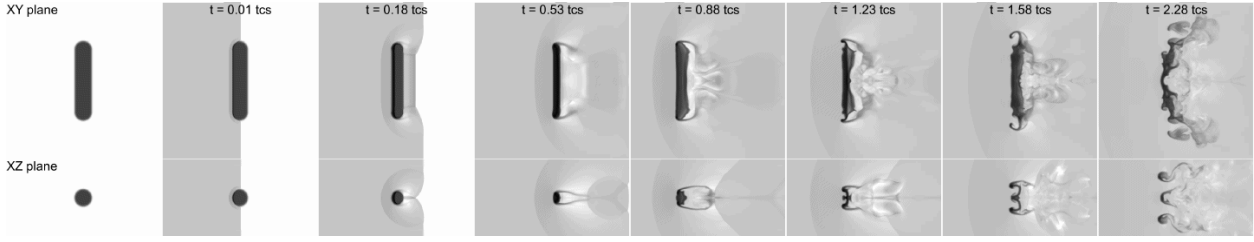


**Figure 3.** Logarithmic density plots of the  $XY$  and  $XZ$  planes as a function of time for simulation *m10c2l8s*. The grayscales shows the logarithm of the mass density, from  $\rho_{\text{amb}}$  (white) to  $5\rho_c$  (black). Each frame is labelled with the time. All frames show  $-10 < Y < 10$  and  $-5 < Z < 5$  (in units of  $r_c$ ). The first 4 frames show  $-10 < X < 10$ , while frames 5–7 show  $-5 < X < 15$  and frame 8 shows  $0 < X < 20$ . The shock is initially at  $X = -10$ .

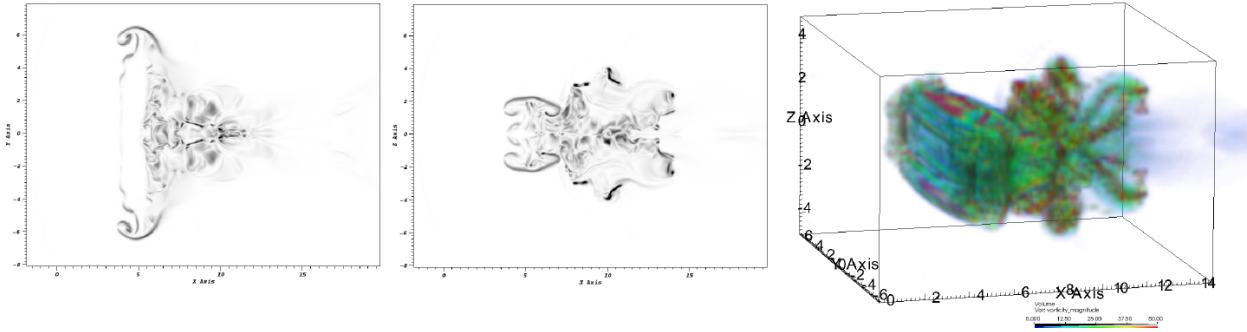


**Figure 4.** The vorticity magnitude in simulation *m10c2l8s* at  $t = 1.58 t_{\text{cs}}$ . a) The  $Z = 0$  plane. b) The  $Y = 0$  plane. c) A 3D volumetric rendering.

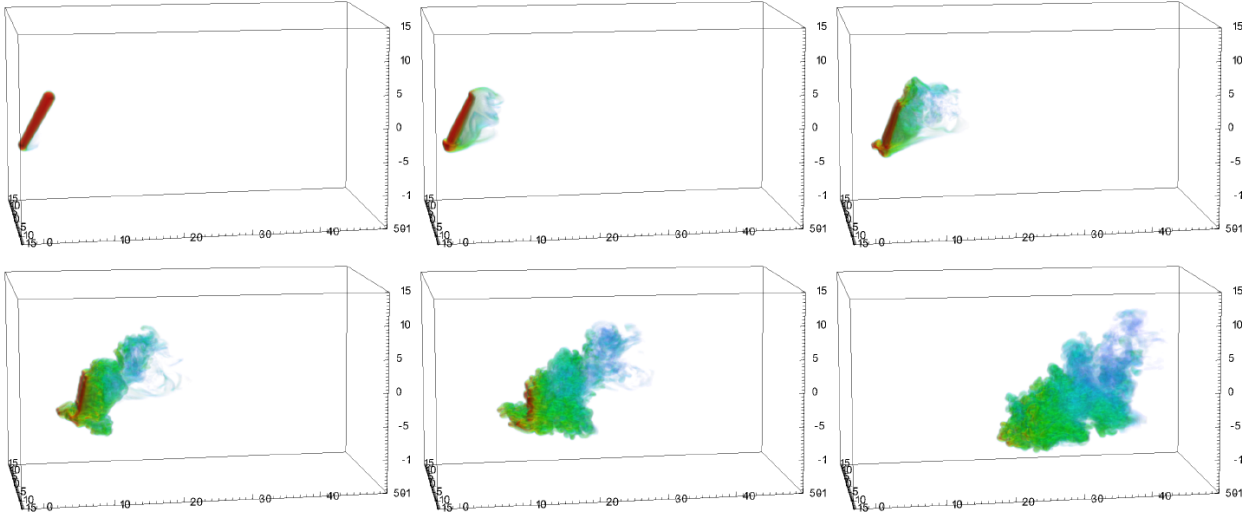


**Figure 5.** As Fig. 1 but for simulation *m10c2l8o30*. Snapshots are at  $t = 0.18, 0.88, 1.58, 2.28, 2.98$  and  $4.37 t_{\text{cs}}$ .  $t_{\text{drag}} = 3.09 t_{\text{cs}}$  and  $t_{\text{mix}} = 4.28 t_{\text{cs}}$ .

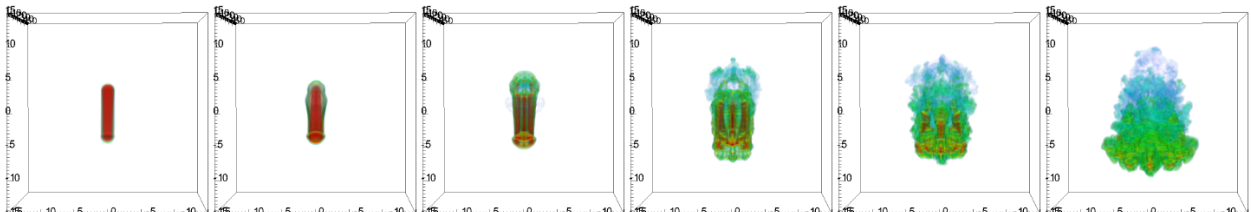


**Figure 6.** As Fig. 5 but viewing from the front.

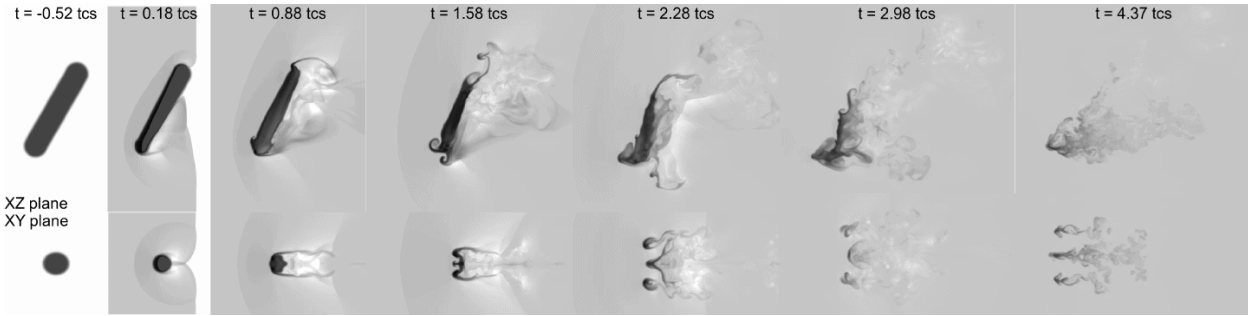


**Figure 7.** Logarithmic density plots of the  $Y = 0$  and  $Z = 0$  (or  $Z = -9$ , for the panel at  $t = 4.37 t_{cs}$ ) planes as a function of time for simulation *m10c2l8o30*. The grayscale shows the logarithm of the mass density, from  $\rho_{amb}$  (white) to  $5\rho_c$  (black). Each frame is labelled with the time. The  $(X, Y, Z)$  extent of the frames (in units of  $r_c$ ) as a function of time are:  $(\pm 5, \pm 5, \pm 10)$  at  $t = -0.52$  and  $0.18 t_{cs}$ ,  $(-5$  to  $10, \pm 5, \pm 10)$  at  $t = 0.88 t_{cs}$ ,  $(-5$  to  $15, \pm 5, \pm 10)$  at  $t = 1.58 t_{cs}$ ,  $(0 - 20, \pm 5, \pm 10)$  at  $t = 2.28 t_{cs}$ ,  $(5 - 30, \pm 6.25, \pm 10)$  at  $t = 2.98 t_{cs}$ , and  $(15 - 46.25, \pm 7.8125, -15$  to  $10)$  at  $t = 4.37 t_{cs}$ . The shock is initially at  $X = -10$ .

grows in size as the filament material becomes increasingly mixed.

Fig. 4 shows the vorticity magnitude in simulation *m10c2l8s* at  $t = 1.58 t_{cs}$ . Vorticity grows at the shear layers on the outside surface of the filament, and becomes very prominent in the wake behind the filament. Vorticity is also produced as the external shock moves around the filament ends and interacts with the shock refracted over the top and bottom of the filament. Later on, the vorticity field is highly intricate, and reflects the complex nature of the interaction.

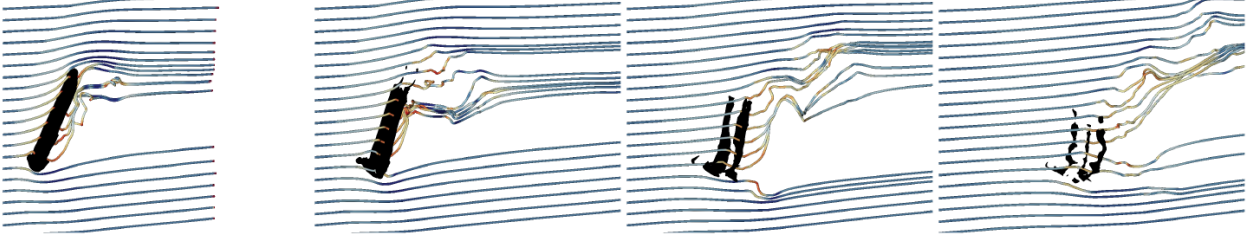
#### 4.1.2 Dependence on the filament orientation

The interaction with an obliquely-oriented filament, specifically simulation *m10c2l8o30*, is shown in Figs. 5-7. Here, the filament's major axis is at a  $30^\circ$  angle to the shock surface. The shock interacts first with the upstream end of the filament, and because of the inclination of the filament the transmitted shock is at an angle to the long axis of the filament. At  $t = 0.18 t_{cs}$ , Fig. 7 shows that the external shock which has swept over the centre of the filament interacts with the shock which is diffracted around the bottom of the filament. The high pressure region which forms behind the filament when the external shock converges on the  $Y = 0$  plane can be seen to drive a transmitted shock into the rear of the filament. A vortex ring forms around the bottom end of the filament (see Figs. 5 and 6) and at  $t = 0.88 t_{cs}$  regions of high vorticity spill around the bottom end of the filament. A RT instability forms at the top of the filament and a wake with turbulent-like characteristics is created downstream of the filament. At  $t = 1.58 t_{cs}$  the most turbulent part of the wake is near the top of the filament, while KH rolls are seen at the bottom. A fragment breaks off the bottom of the filament by  $t = 2.28 t_{cs}$ . The wake extends above and downstream of the filament, and behind the broken off fragment, and appears to become increasingly “turbulent” with time. Periodic vortex shedding occurs off the top part of the filament, due to the high pressure on the upstream side of the filament leaking around the end of the filament. This is highlighted in Fig. 8 which shows a number of eddies forming and being advected downstream. As a result of its initial orientation, the filament as a whole is pushed downwards by the passage of the shock and the subsequent post-shock flow. The face-on view displayed in Fig. 6 and the

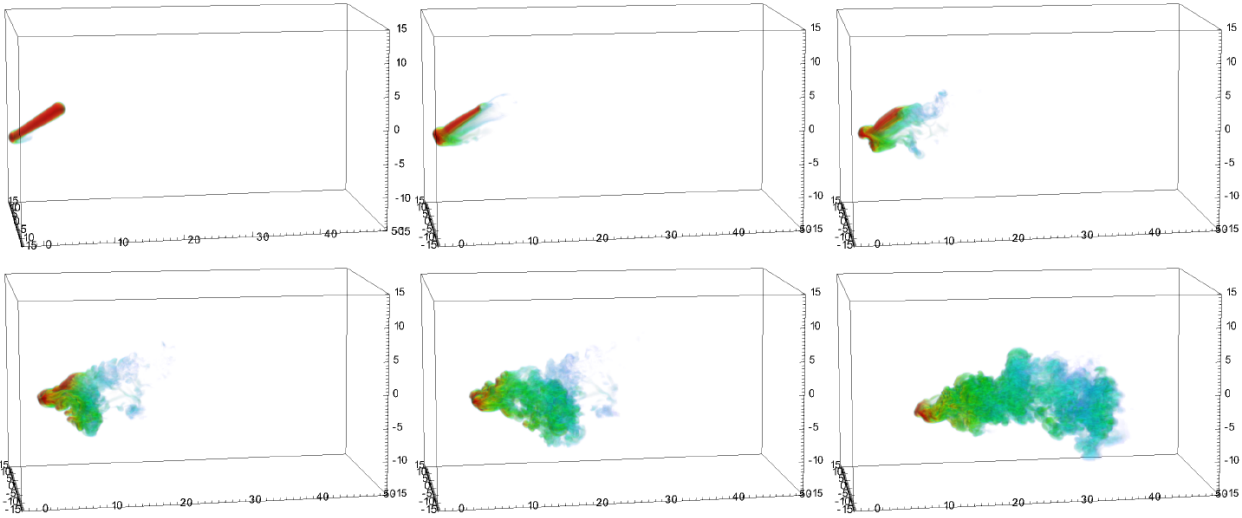
density plots in the  $XY$  plane displayed in the part bottom of Fig. 7 show again that the filament breaks into 3 parallel rolls. Comparison with the reference simulation reveals that the interaction has major differences at all stages. At late times the wake is also noticeably longer than that in simulation *m10c2l8s*.

Fig. 9 shows streamlines in simulation *m10c2l8o30* at 4 different snapshots in time. The densest part of the filament is highlighted by the black surface. The flow around the filament is clearly complex. In the top left panel the streamlines end at the shock towards the right of the plot. Moving along the streamlines from left to right, the first change in colour and/or direction of the streamlines indicates the position of the bowshock upstream of the filament, with the postshock flow being slower and typically changed in direction. On the upstream side of the filament the streamlines bend upwards as the flow attempts to move around the filament. The flow also accelerates around the bottom and top ends of the filament, indicated by a darker blue colour to the streamlines at this point. The wake behind the filament is complex, with the velocity along some streamlines showing abrupt changes in velocity and direction. A vortex, indicated by spiralling streamlines, is visible downstream of the top part of the filament. There is also a clear gap in the downstream wake where no streamlines exist. This indicates that the flow in this region originally originated from outside the  $Y = 0$  plane. Similar flow behaviour is seen in the other panels. The viewpoint is the same for all panels, so the downstream movement of the filament can be appreciated. In the final panel we see the filament has fragmented into 3 parts (cf. Figs 5-7).

Figs. 10 and 11 show the nature of the interaction when the filament is inclined yet further to the shock (specifically simulation *m10c2l8o60*). The main difference to simulation *m10c2l8o30* is that the filament does not form into 3 parallel rolls. Instead, the vortex ring which forms at the upstream end of the filament is more dominant, and is asymmetric around the filament because of the filament's inclination. This causes the filament to fragment from the bottom, but the larger fragments are from the top part of the ring. Comparing Figs. 1, 5 and 10 we see a further extension in the length of the wake at late times. This is because the filament loses mass more slowly and has a longer lifetime than those in simulations *m10c2l8s* and *m10c2l8o30* (see Fig. 28c). The



**Figure 9.** Streamlines in simulation *m10c2l8o30* at  $t = 0.88, 1.58, 2.28$  and  $2.98 t_{cs}$ . The streamlines are in the  $Y = 0$  plane and are introduced at  $X = -5$ . They are colour coded with the velocity from dark red (low speed) to dark blue (high speed). The black surface is a contour at the original filament density.



**Figure 10.** As Fig. 1 but for simulation *m10c2l8o60*. Snapshots are at  $t = 0.18, 0.88, 1.58, 2.28, 2.98$  and  $4.37 t_{cs}$ .  $t_{drag} = 4.59 t_{cs}$  and  $t_{mix} = 5.00 t_{cs}$ .

wake also has a smaller transverse cross-sectional area than seen in the previous simulations.

In Figs. 12, 13 and 14 we show the interaction of a shock with a filament which is almost end-on to the shock (simulation *m10c2l8o85*). The transmitted shock into the filament now moves along its length, as does the vortex ring formed at its upstream end. However, the transmitted shock is  $\approx 10\times$  slower than the external shock, so that shocks are also driven into the filament from its sides before the end-transmitted shock has had time to move very far along the filament length. These “side” shocks move almost perpendicular to the long filament axis. They pass through the centre of the filament at  $\sim 0.5 - 0.6 t_{cs}$ . Shortly after this they reach the opposite surface and cause rarefaction waves which move back towards the filament’s central axis. This results in the dramatic “hollowing” or “voiding” of the filament, seen most prominently at  $t = 1.23 t_{cs}$  in Fig. 14. At about this time, the vortex ring triggers the destruction of the upstream end of the filament, exposing material further along the length of the filament to the external flow. This material then fragments as non-azimuthal instability modes grow. Note that the filament is almost completely destroyed before the transmitted shock has passed all the way through it, which doesn’t happen until  $t \approx 5 t_{cs}$  (the transmitted shock can be seen just downstream of the “head” of the filament at  $t = 1.23, 1.58$  and  $2.28 t_{cs}$  in Fig. 14). Again, the

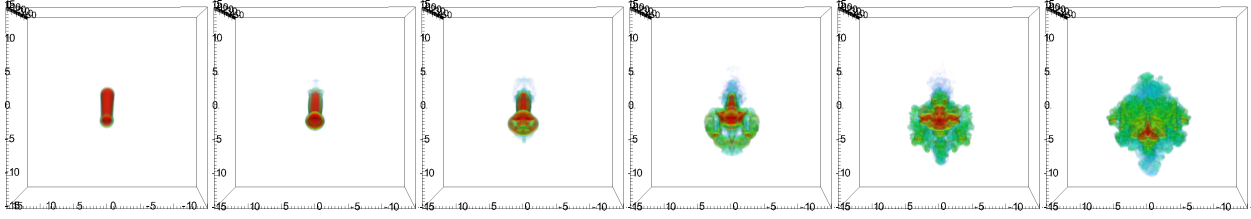
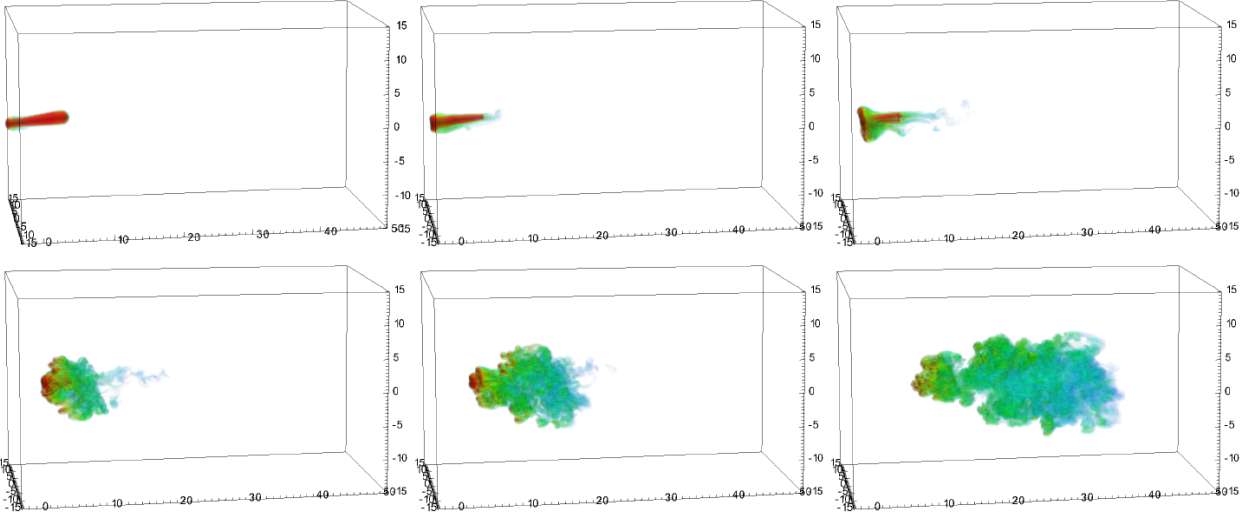
filament wake has a relatively compact cross-section. The  $XZ$  and  $XY$  snapshots shown in Fig. 14 also reveal how the initial interaction differs when the long-axis of the filament is at a small angle to the shock normal (as in the  $XZ$  plane), as compared to exactly aligned with it (as in the  $XY$  plane).

#### 4.1.3 Dependence on filament length

The 3 parallel rolls seen in simulation *m10c2l8s* are a striking feature. Since spherical clouds do not break up in this way, we wish to determine what length of filament is needed for these rolls to form. Figs. 15 and 16 show results from simulation *m10c2l2s*, where  $l$  is reduced to 2. It is clear that 3 parallel rolls still form, and the filament morphology evolves in a broadly similar way to that in simulation *m10c2l8s*.

It is also interesting to see how shorter filaments respond when they have an oblique orientation to the shock. Figs. 17 and 18 show results from simulation *m10c2l4o30*, where  $l = 4$  and  $\theta = 30^\circ$ . This simulation also develops 3 parallel rolls, in keeping with simulations *m10c2l4s* and *m10c2l8o30*. Reducing  $l$  to 2 and keeping  $\theta = 30^\circ$ , for the first time (when  $\theta < 60^\circ$ ) we find that the interaction does not develop 3 parallel rolls - see Figs. 19 and 20 - in contrast to simulations *m10c2l2s* and *m10c2l4o30*.



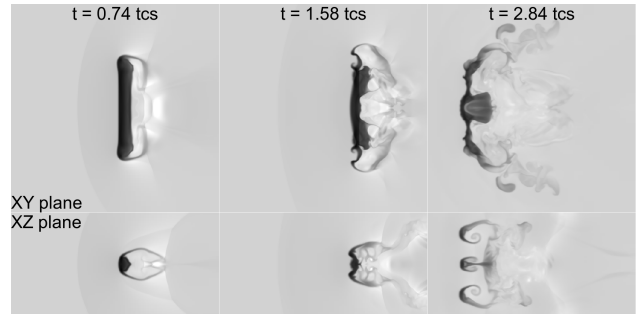
**Figure 11.** As Fig. 10 but viewing from the front.**Figure 12.** As Fig. 1 but for simulation *m10c2l8o85*. Snapshots are at  $t = 0.18, 0.88, 1.58, 2.28, 2.98$  and  $4.37 t_{cs}$ .  $t_{drag} = 4.03 t_{cs}$  and  $t_{mix} = 4.33 t_{cs}$ .

#### 4.1.4 Mach number dependence

All the results shown so far have involved a Mach 10 shock. Previous work on shocks interacting with spherical clouds has revealed that the interaction is milder, and that instabilities develop more slowly, when the Mach number of the shock is reduced. We now wish to see how this behaviour translates to a shock interacting with a filament.

Fig. 21 shows the interaction of a Mach 3 shock with a  $\chi = 10^2$ , sideways-oriented filament (simulation *m3c2l8s*). The interaction is less “violent” compared to simulations with higher Mach numbers (e.g., simulation *m10c2l8s* shown in Figs. 1-3). The transmitted shock moves into the filament relatively quicker, which changes the timing and position of secondary shocks and rarefactions within the filament, and its reverberations. The post-shock compression is reduced, as is the velocity shear over the filament. In particular, it takes longer to form the 3 parallel rolls (compare the frames at  $t = 1.58 t_{cs}$ ), though they still appear later. Nevertheless, the interaction proceeds broadly as before.

A further reduction in the Mach number to 1.5 yields a still gentler interaction (see Fig. 22). The external post-shock flow is now subsonic with respect to the filament, so a bow-wave rather than a bow-shock forms upstream. The flow around the filament appears much more laminar, as can be seen from the large eddies present in the filament wake in the  $XZ$  plane at  $t = 0.38 t_{cs}$ . The drag and mixing timescales are both much increased.

**Figure 21.** Logarithmic density plots of the  $XY$  and  $XZ$  planes as a function of time for simulation *m3c2l8s*. The grayscale shows the logarithm of the mass density, from  $\rho_{amb}$  (white) to  $5\rho_c$  (black). Each frame is labelled with the time. All frames show  $-10 < Y < 10$  and  $-5 < Z < 5$  (in units of  $r_c$ ). The first two frames show  $-10 < X < 10$ , while the last shows  $5 < X < 25$ . The shock is initially at  $X = -10$ .  $t_{drag} = 3.27 t_{cs}$  and  $t_{mix} = 4.23 t_{cs}$ .

#### 4.1.5 Dependence on density contrast

We now examine how the interaction changes with the density contrast of the filament. All results so far have been for filaments with  $\chi = 10^2$ . In the interaction of a shock with a spherical cloud, increasing the density contrast creates a more “resistant” obstacle, which accelerates more slowly ( $t_{drag} \propto \chi^{1/2} t_{cc}$ ) and which is subject to increased KH instabilities and hydrodynamic ablation - decreasing  $\chi$  has

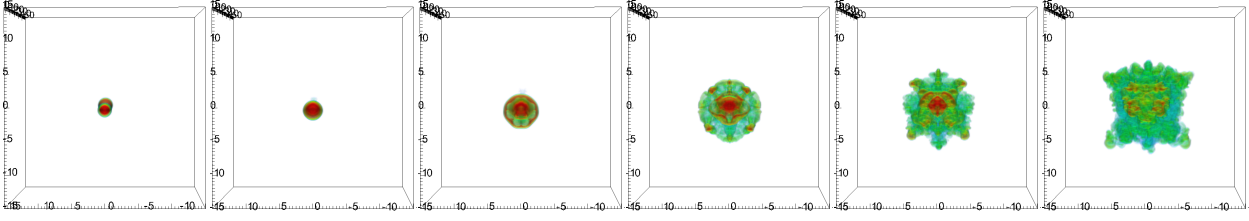


Figure 13. As Fig. 10 but viewing from the front.

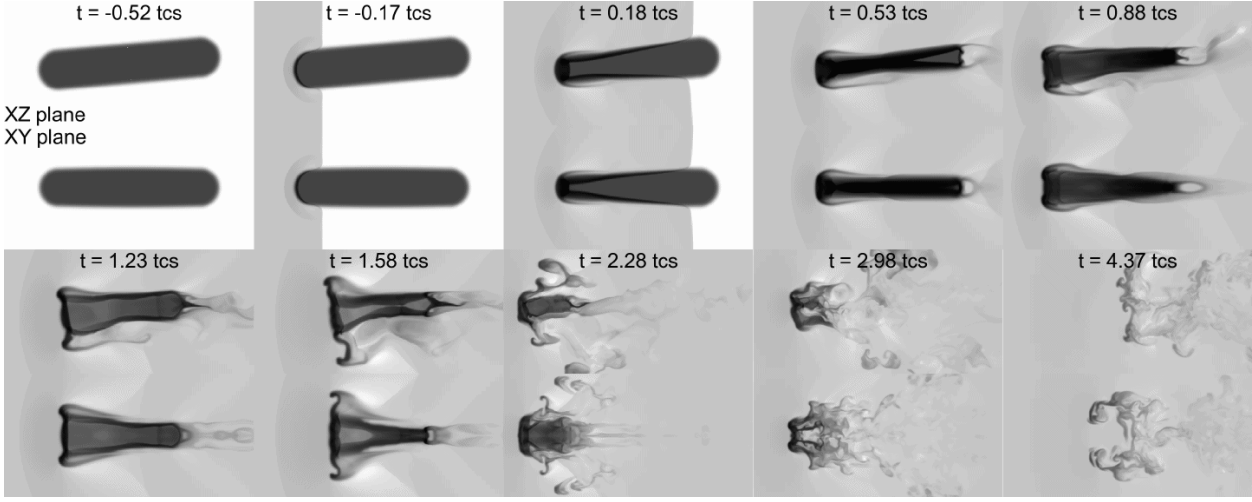


Figure 14. Logarithmic density plots of the  $Y = 0$  and  $Z = 0$  planes as a function of time for simulation *m10c2l8o85*. The grayscales shows the logarithm of the mass density, from  $\rho_{\text{amb}}$  (white) to  $5\rho_c$  (black). Each frame is labelled with the time. The  $(X, Y, Z)$  extent of the frames (in units of  $r_c$ ) as a function of time are:  $(\pm 3.5, \pm 3.5, \pm 7)$  at  $t = -0.52, -0.17, 0.18$  and  $0.53 t_{\text{cs}}$ ,  $(-5 \text{ to } 9, \pm 3.5, \pm 3.5)$  at  $t = 0.88, 1.23$  and  $1.58 t_{\text{cs}}$ , and  $(0 \text{ to } 20, \pm 5, \pm 5)$  at  $t = 2.28, 2.98$  and  $4.37 t_{\text{cs}}$ . The shock is initially at  $X = -10$ .

the opposite effect (see, e.g., Pittard et al. 2010; Pittard & Parkin 2016).

Fig. 23 shows the effect of reducing  $\chi$  to 10 (simulation *m10c1l8s*). The transmitted shock moves much faster through the filament relative to the speed of the external shock in this case (it is  $\approx 3\times$  slower). The filament experiences a much faster acceleration downstream, and becomes quite thin (see the panel at  $t = 1.91 t_{\text{cs}}$  in Fig. 23). At  $t = 1.91 t_{\text{cs}}$ , we see that shocks exist in the external flow either side of the filament, in addition to the bowshock further upstream. These are caused by the transmitted shocks exiting the filament, and accelerating into the lower density surrounding flow.

Fig. 24 shows the effect of increasing  $\chi$  to  $10^3$  (simulation *m10c3l8s*). The filament now accelerates downstream more slowly, and is subject to stronger instabilities. Many more shocks are present in the wake. The filament evolution is however much more akin to that in simulation *m10c2l8s* than in *m10c1l8s*. Note that the resolution of *m10c3l8s* is  $R_{16}$ , whereas all our other simulations are at  $R_{32}$ .

Finally, we examine the interaction of low Mach number shocks with low density contrast filaments. Fig. 25 shows results from simulation *m3c1l8s*, with  $M = 3$  and  $\chi = 10$ . Key features are the double bow-shocks seen upstream at  $t = 1.21 t_{\text{cs}}$  and the large-scale eddies seen in the  $XZ$  plane. There is general similarity with simulation *m10c1l8s* (see Fig. 23). Fig. 26 shows the interaction in simulation *m1.5c1l8s*, with  $M = 1.5$  and  $\chi = 10$ . Again a bow-wave

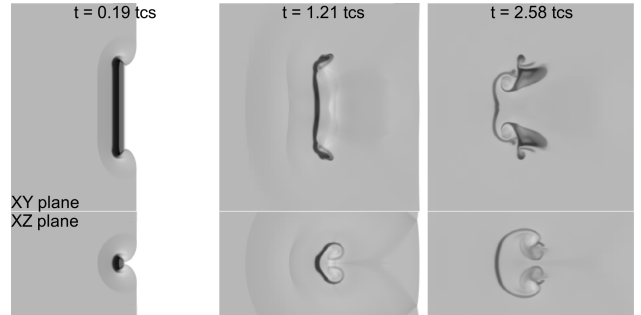
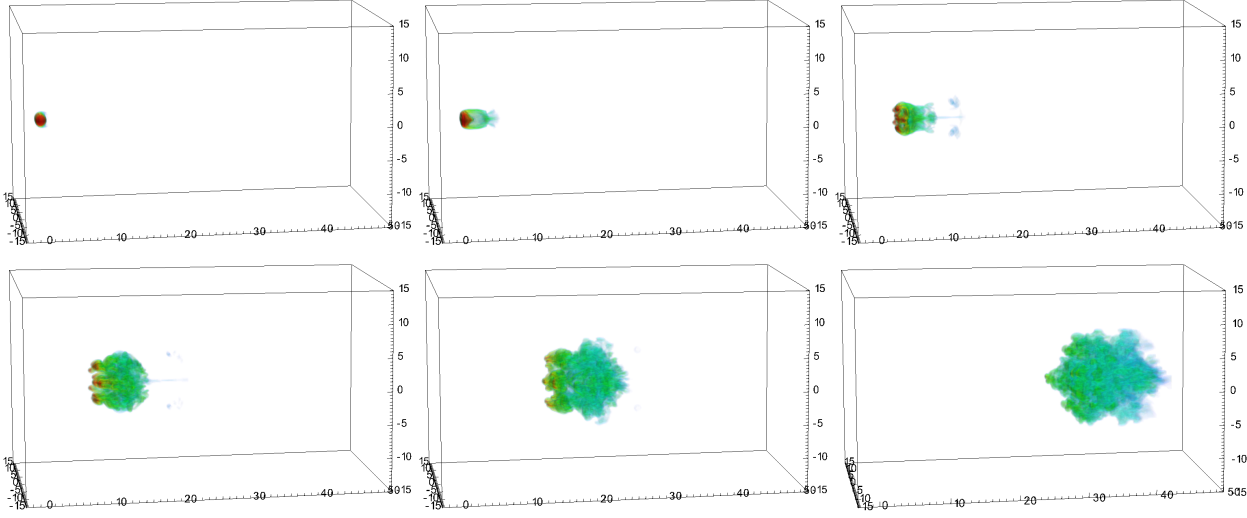


Figure 25. Logarithmic density plots of the  $XY$  and  $XZ$  planes as a function of time for simulation *m3c1l8s*. The grayscales shows the logarithm of the mass density, from  $\rho_{\text{amb}}$  (white) to  $5\rho_c$  (black). Each frame is labelled with the time. All frames show  $-10 < Y < 10$  and  $-5 < Z < 5$  (in units of  $r_c$ ). From left to right the frames show  $-10 < X < 10$ ,  $-5 < X < 15$  and  $5 < X < 25$ . The shock is initially at  $X = -10$ .  $t_{\text{drag}} = 1.51 t_{\text{cs}}$  and  $t_{\text{mix}} = 4.83 t_{\text{cs}}$ .

forms upstream. The flow around the filament appears to be the most laminar yet, due to the gentleness of the interaction and the rapid acceleration of the filament up to the postshock speed.

Fig. 27 shows the vorticity magnitude in simulation *m1.5c1l8s*. Here the vorticity magnitude highlights the main dynamical feature of this flow which is the symmetric pair of vortices produced in the filament wake. At this stage of



**Figure 15.** As Fig. 1 but for simulation *m10c2l2s*. Snapshots are at  $t = 0.26, 1.26, 2.26, 3.26, 4.26$  and  $6.26 t_{cs}$ .  $t_{\text{drag}} = 3.13 t_{cs}$  and  $t_{\text{mix}} = 4.20 t_{cs}$ .

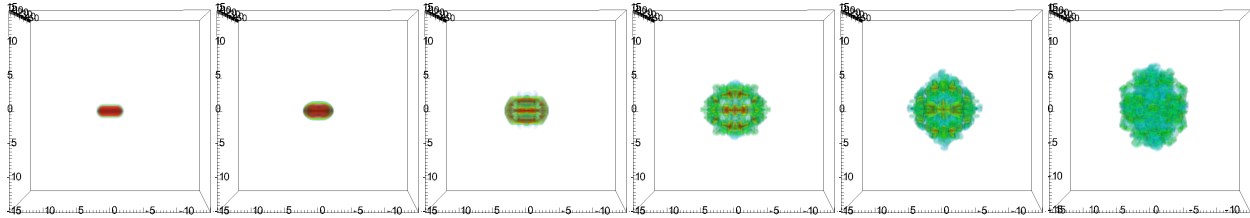


**Figure 16.** As Fig. 15 but viewing from the front.

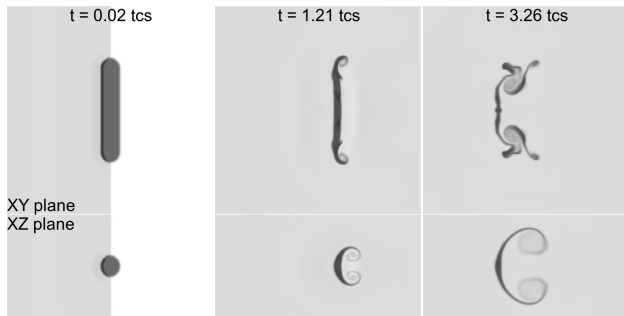


**Figure 26.** Logarithmic density plots of the  $XY$  and  $XZ$  planes as a function of time for simulation *m1.5c1l8s*. The grayscale shows the logarithm of the mass density, from  $\rho_{\text{amb}}$  (white) to  $5\rho_c$  (black). Each frame is labelled with the time. All frames show  $-10 < Y < 10$  and  $-5 < Z < 5$  (in units of  $r_c$ ). The first two frames show  $-10 < X < 10$ , while the third frame shows  $0 < X < 20$ . The shock is initially at  $X = -10$ .  $t_{\text{drag}} = 3.33 t_{cs}$  and  $t_{\text{mix}} = 13.1 t_{cs}$ .

the interaction the flow in the  $Y = 0$  plane is mostly 2D. We can estimate an effective Reynold's number for the 2D flow on our grid as  $Re \sim (\eta/l)^{-2}$ . Here, the largest eddy has a size  $l \sim R_c$ , while the smallest eddies have a size  $\eta \sim 2\Delta x = R_c/16$ . Hence we obtain  $Re \sim 250$ . If the filament were a rigid structure one might expect to see vortex shedding for this value of  $Re$  (see discussion in Sec. 4.1.6). The fact that we don't see this is likely due to the non-

rigidity of the filament (which becomes significantly distorted as a result of these vortices) and its acceleration with the flow.

#### 4.1.6 Comparison to Flow Past a Rigid Cylinder

As our work resembles flow past a cylinder of circular cross-section it is worth examining what is known about such flows in general. Flow around a cylinder of circular cross-section has many important applications in engineering and is well studied by the engineering and fluid dynamics communities. The behaviour of an incompressible fluid flowing past an infinite cylinder is known to be a strong function of the Reynolds number (see, e.g., the review by Williamson 1996). The flow is steady and laminar for  $Re \lesssim 50$ , and the wake contains a recirculation region with two symmetrically placed vortices. The wake displays von Karman vortex shedding for  $100 \lesssim Re \lesssim 200$ . 3D instabilities start to appear at  $Re \sim 200$  and low levels of turbulence start to develop within the vortices by  $Re \sim 400$ . For high  $Re (\sim 10^5)$ , the turbulence spreads out of vortices and a fully turbulent wake is formed (see, e.g., Davidson 2004). The roughness of the cylinder and the flow quality (the turbulence levels in the oncoming flow, as well as the character of this turbulence), also affect the flow dynamics (Williamson 1996).

The flow past finite-length cylinders has also been studied. Experiments by Park & Lee (2000) show that the flow past the free-end of a finite cylinder has a complicated 3D wake structure when  $Re = 2 \times 10^4$ . The wake is affected by



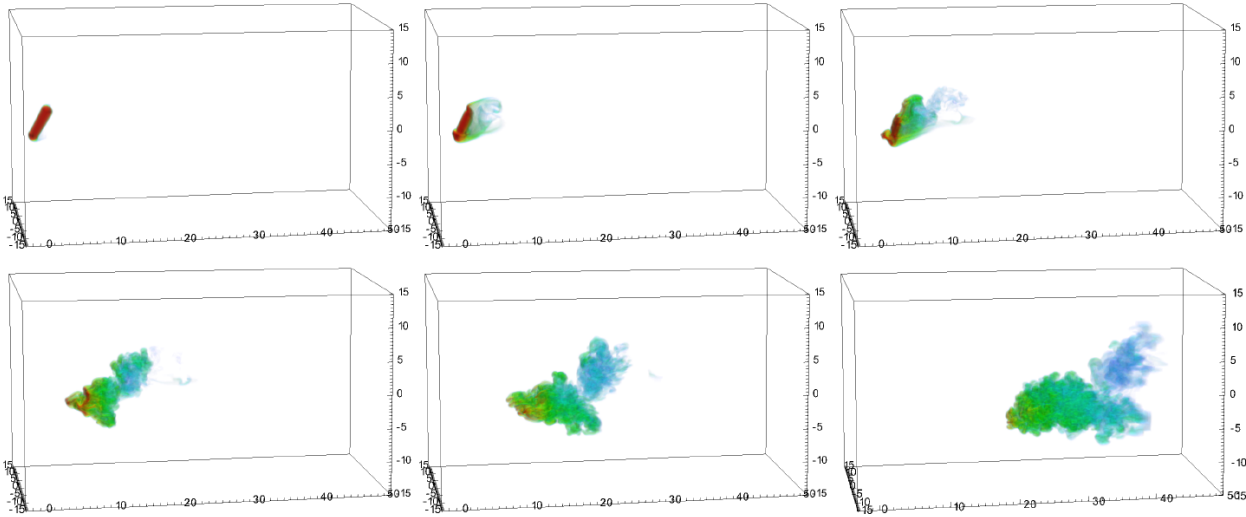


**Figure 17.** As Fig. 1 but for simulation *m10c2l4o30*. Snapshots are at  $t = 0.23, 1.08, 1.93, 2.79, 3.64$  and  $5.35 t_{cs}$ .  $t_{drag} = 3.82 t_{cs}$  and  $t_{mix} = 4.83 t_{cs}$ .

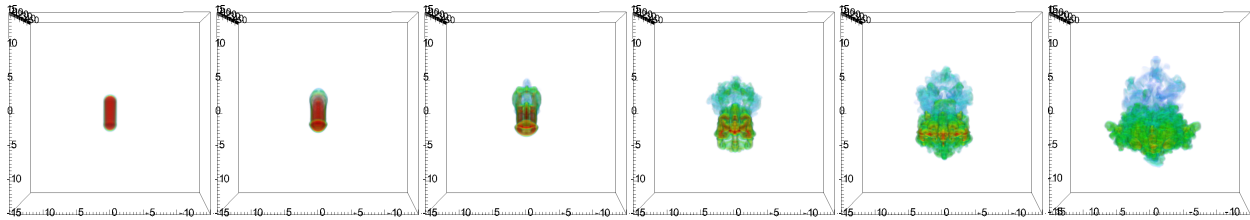


**Figure 18.** As Fig. 17 but viewing from the front.

the downwash of counter-rotating vortices separated from the free end. Other experiments reveal that as the height-to-diameter ratio ( $H/D$ ) of the cylinder is reduced, the regular alternating vortex shedding is replaced more and more by symmetrically shed vortices in the range  $2 \lesssim H/D \lesssim 6$ , and is mostly suppressed for  $H/D \lesssim 2$  (Okamoto & Yagita 1973; Kawamura et al. 1984; Kappler 2002). Large eddy simulations by Fröhlich & Rodi (2004) investigated the behaviour at  $Re = 4.3 \times 10^4$  of flow past a cylinder with  $H/D = 2.5$ . These authors find that the relatively small height of the cylinder causes the 2D von Karman vortices to bend and distort as they travel along the wake. An arch-type vortex is also seen in the average (but not the instantaneous) flow behind the cylinder.

Early theoretical and experimental research on inclined (or yawed) cylinders attempted to associate the flow to that of a non-yawed cylinder experiencing the flow component normal to the cylinder axis (see references in Zdravkovich 2003). The validity of this “Independence Principle” or “Cosine Law” has been assessed by Ramberg (1983), amongst others. Experiments by Shirakashi et al. (1986) and Matsumoto et al. (1990) determined an axial flow on the leeward surface, while Larose et al. (2003) investigated the effects of both  $Re$  and the inclination angle. The experimental studies are now complemented by numerical simulations of the flow around inclined cylinders, which cover a wide range of  $Re$  (e.g., Yeo & Jones 2008; Vakil & Green 2009).

Though these works are interesting and have some relevance to our work, the differences which exist between them

and our work makes it difficult to conduct a detailed comparison. Our simulations are different from flow past a finite circular cylinder in the following ways: 1) our filament is not rigid (this requires very high  $\chi$ ); 2) our interaction involves a shock and not a wind/flow; 3) the tip of our filament is rounded and not flat; 4) our filament has a rough surface; 5) our interaction is simulated at a lower  $Re$  than many experiments/simulations in the fluid dynamics community; 6) we simulate compressible rather than incompressible flow (Mach numbers of  $M \lesssim 0.1$  are needed for a compressible flow to behave similarly to an incompressible flow, but even for our lowest Mach number simulations with  $M = 1.5$  the Mach number of the post-shock flow is 0.511). For this last reason, our most relevant simulation is probably *m1.5c2l8s*. It indeed shows regular vortices on the two sides of the cylinder. However, since it is not rigid the filament deforms in the flow, which is probably why we do not see vortex shedding.

We can also compare the streamline plots shown in Fig. 9 to Fig. 11 in Vakil & Green (2009), where streamlines around a finite inclined rigid cylinder are shown. The flow in our simulations is clearly more complex, owing to i) the higher effective Reynolds number of our simulation; ii) the compressibility of our flow; iii) the dynamic behaviour and flexibility of our object.

In Sec. 4.3 we compare how  $t_{drag}$  for our filament can be related to the drag coefficient measured for rigid cylinders, and how these quantities vary as  $H/D$  and the orientation of the filament/cylinder change.

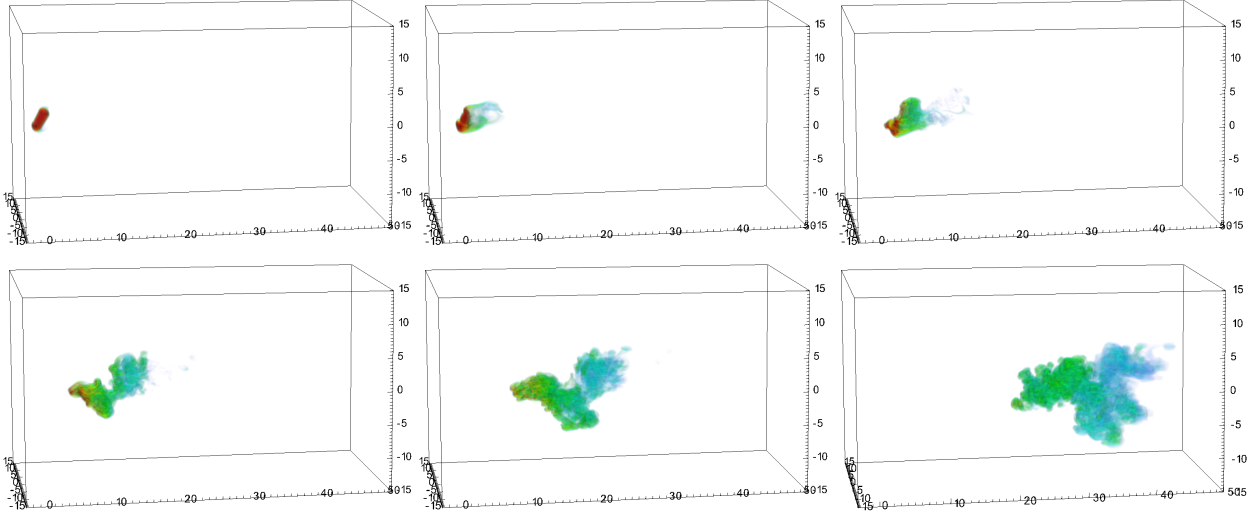


**Figure 19.** As Fig. 1 but for simulation *m10c2l2o30*. Snapshots are at  $t = 0.26, 1.26, 2.26, 3.26, 4.26$  and  $6.26 t_{cs}$ .  $t_{drag} = 3.86 t_{cs}$  and  $t_{mix} = 4.77 t_{cs}$ .

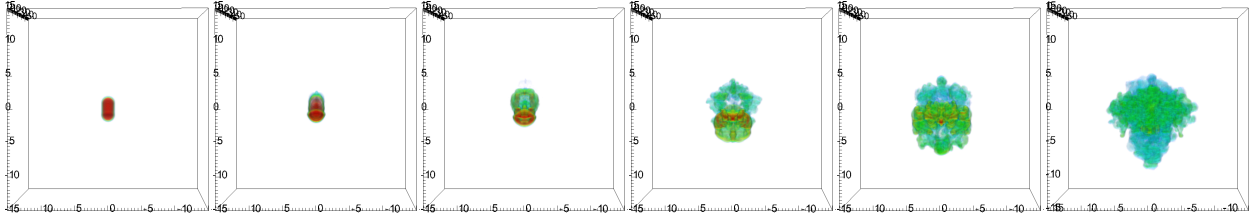


**Figure 20.** As Fig. 15 but viewing from the front.

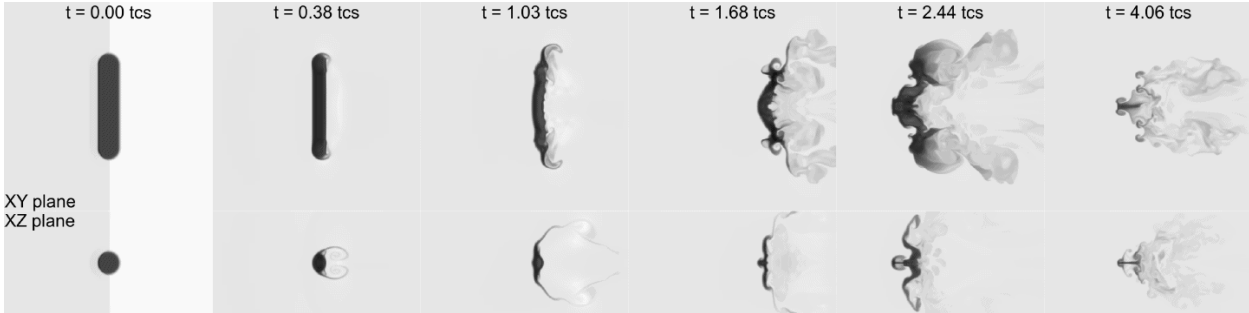


**Figure 22.** Logarithmic density plots of the XY and XZ planes as a function of time for simulation *m1.5c2l8s*. The grayscale shows the logarithm of the mass density, from  $\rho_{amb}$  (white) to  $5\rho_c$  (black). Each frame is labelled with the time. All frames show  $-10 < X < 10$ ,  $-10 < Y < 10$  and  $-5 < Z < 5$  (in units of  $r_c$ ). The shock is initially at  $X = -10$ .  $t_{drag} = 8.30 t_{cs}$  and  $t_{mix} = 8.45 t_{cs}$ .

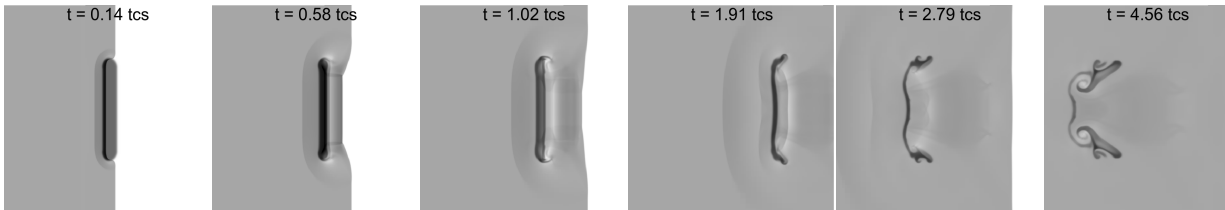


**Figure 23.** Logarithmic density plots of the XY plane as a function of time for simulation *m10c1l8s*. The grayscale shows the logarithm of the mass density, from  $\rho_{amb}$  (white) to  $5\rho_c$  (black). Each frame is labelled with the time. All frames show  $-10 < Y < 10$  (in units of  $r_c$ ). The first 4 frames show  $-10 < X < 10$ , while the sixth shows  $0 < X < 20$ . The final frame shows  $10 < X < 30$ . The shock is initially at  $X = -10$ .  $t_{drag} = 1.10 t_{cs}$  and  $t_{mix} = 5.22 t_{cs}$ .

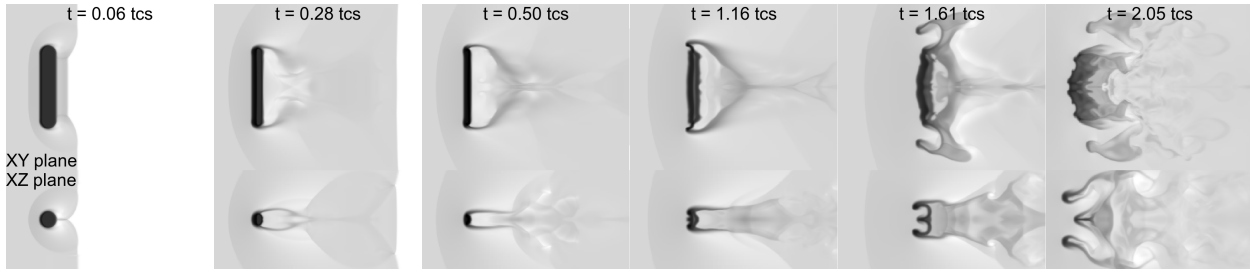


**Figure 24.** Logarithmic density plots of the XY plane as a function of time for simulation *m10c3l8s*. The grayscales shows the logarithm of the mass density, from  $\rho_{\text{amb}}$  (white) to  $5\rho_c$  (black). Each frame is labelled with the time. The first 5 frames show  $-5 < X < 20$ ,  $-10 < Y < 10$ ,  $-6 < Z < 6$  (in units of  $r_c$ ). The final frame shows  $5 < X < 35$ ,  $-12 < Y < 12$ ,  $-7.5 < Z < 7.5$ . The shock is initially at  $X = -10$ .  $t_{\text{drag}} = 3.12 t_{\text{cs}}$  and  $t_{\text{mix}} = 3.33 t_{\text{cs}}$ .

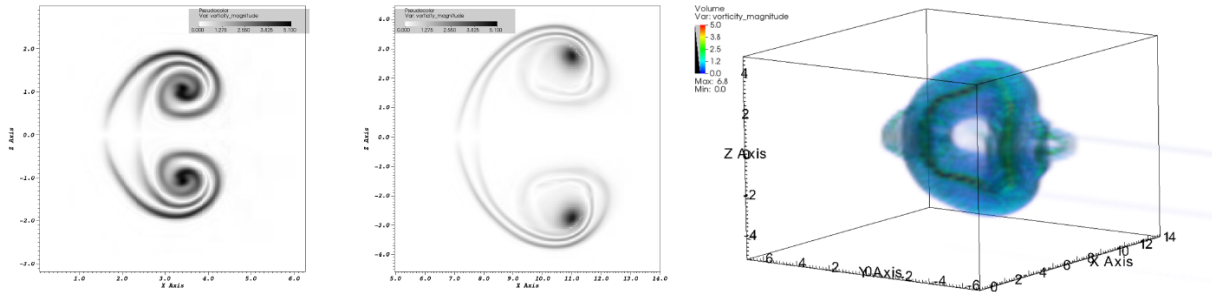


**Figure 27.** The vorticity magnitude in simulation *m1.5c1l8s* at  $t = 1.21$  (left) and  $3.26 t_{\text{cs}}$  (middle and right).

## 4.2 Statistics

In this section we examine the evolution of some key global quantities of the interaction. Our initial focus is on simulations with  $M = 10$  and  $\chi = 10^2$ : other Mach numbers and density contrasts are examined later.

We first consider the evolution of  $m_{\text{core}}$ , the “core” mass of the filament.  $m_{\text{core}}$  declines as material is stripped from the filament and mixes into the surrounding flow. For spherical clouds, the mixing time,  $t_{\text{mix}}$ , defined as the time when  $m_{\text{core}}$  reaches half of its initial value, is  $\approx 6 t_{\text{cc}}$  for reasonably sharp-edged clouds at high Mach numbers, and increases quite strongly at lower Mach numbers (Pittard et al. 2010; Pittard & Parkin 2016).

Fig. 28 shows the evolution of  $m_{\text{core}}$  for simulations with  $M = 10$  and  $\chi = 10^2$ , as a function of the filament length and initial orientation. The evolution is normalized in terms of  $t_{\text{cc}}$  (top row),  $t'_{\text{cc}}$  (middle row), and  $t_{\text{cs}}$  (bottom row). Results for a spherical cloud are also shown. In terms of  $t_{\text{cc}}$ , the greater mass of a filament compared to a spherical cloud means that  $m_{\text{core}}$  declines more slowly as  $l$  increases (see, e.g., Figs. 28a and b). This is true irrespective of the filaments orientation. On the other hand, Fig. 28c) shows that filaments oriented sideways on to the shock initially lose mass most rapidly, while mass-loss is delayed for the filaments which are most oblique (*m10c2l8o60* and *m10c2l8o85*). This is likely due to the fact that it takes longer for the shock to sweep over these filaments (in simulation *m10c2l8o85* the long axis of the filament is almost aligned with the shock normal - see Fig. 12). However, it is interesting to discover that the final 20% of the mass-loss from the sideways on filament occurs

more gradually<sup>2</sup>, and that filaments oriented at an angle of  $60^\circ$  to the shock front lose mass more slowly than those at other orientations. In the former instance this is likely because these filaments are accelerated more rapidly, and thus the velocity shear which is responsible for driving the mixing is reduced. However, it is not obvious why a  $60^\circ$  orientation slows the rate of stripping.

We find that there is a general reduction in the variance between the simulations when the evolution is measured in units of  $t'_{\text{cc}}$ . In particular, the rate of decline in  $m_{\text{core}}$  becomes similar for all simulations, and there is less spread in the time at which  $m_{\text{core}}$  nears zero. A further tightening of the curves occurs when the evolution is measured in units of  $t_{\text{cs}}$  (see panels d) and g) in Fig. 28). For the rest of this work, therefore, we present our results with the timescale normalized by  $t_{\text{cs}}$ .

With the time normalized by either  $t'_{\text{cc}}$  or  $t_{\text{cs}}$ , Figs. 28d) and g) reveal that filaments side-on to the shock are destroyed *more* rapidly than spherical clouds of the same mass. This is a result of the greater surface area to volume ratio of the filaments. The destruction timescale reduces with increasing filament length in such cases. Note that the difference between the spherical and *m10c2l2s* simulations is greater than that between the *m10c2l2s* and *m10c2l8s* simulations, indicating that even a small change from sphericity can significantly affect the destruction process. Similar behaviour is observed for oblique filaments (though the filament with  $l = 4$  takes slightly longer than expected for

<sup>2</sup> This is also seen in the MHD interaction of a filament with a parallel shock (Goldsmith & Pittard 2016).

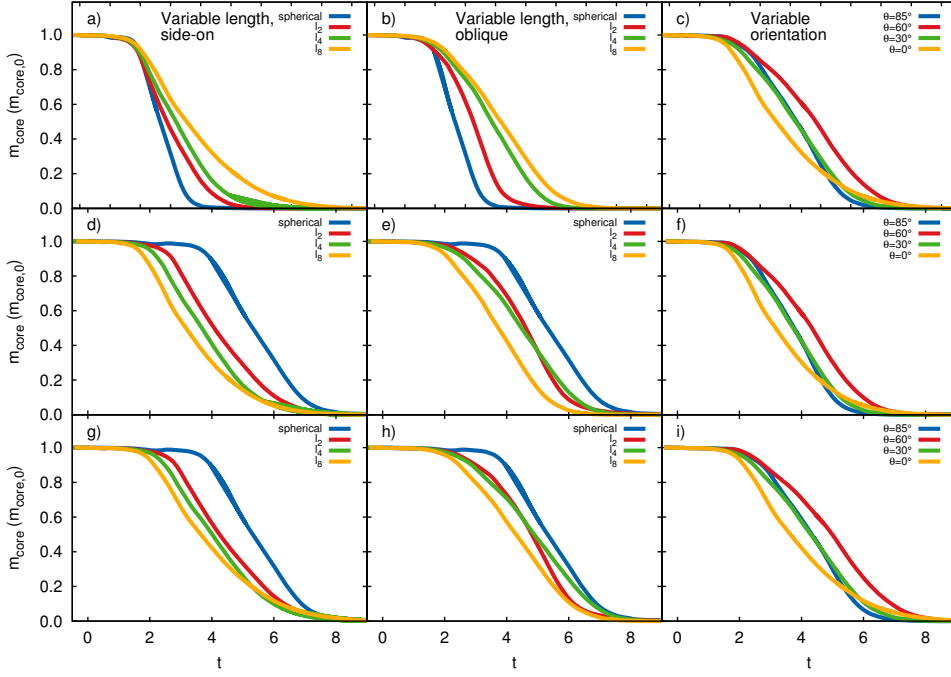


**Figure 28.** Time evolution of the core mass,  $m_{\text{core}}$ , normalized to its initial value, for various simulations with  $M = 10$  and  $\chi = 10^2$ . The left panels are for “side-on” simulations, the centre panels are for simulations with  $\theta = 30^\circ$ , while the right panels are for filaments with  $l = 8$ . The evolution is normalized in terms of  $t_{cc}$  (top row),  $t'_{cc}$  (middle row), and  $t_{cs}$  (bottom row). The best convergence is achieved when  $t_{cs}$  is used to normalize the time.

the final 50% of its core mass to be mixed into the ambient flow).

The time evolution of the  $X$  and  $Z$  centre-of-mass position of the filament ( $\langle x \rangle_{\text{cloud}}$  and  $\langle z \rangle_{\text{cloud}}$ , respectively) for various simulations is shown in Fig. 29. We see that longer filaments are accelerated faster and move downstream more rapidly than shorter filaments, when the time is normalized by  $t_{cs}$ . This is again because of their greater surface-area to volume ratio (shorter filaments are closer to sphericity), and is also again independent of the initial filament orientation. For filaments of fixed length, Fig. 29c) shows that sideways on filaments are accelerated faster downstream. Filaments with  $\theta = 85^\circ$  are accelerated slightly faster than those with  $\theta = 60^\circ$ , which is probably due to the transmitted shock moving through the filament in a direction very close to the normal of the incident shock.

The movement of the filament in the  $Z$ -direction is shown in Fig. 29d-f). Due to the symmetry, there is no significant movement of the filament in the  $Z$ -direction for sideways on filaments (see Fig. 29d). However, filaments with  $\theta = 30^\circ$  are pushed downwards by the shock and the post-shock flow. The longer filaments feel this downwards force for longer and so experience a larger displacement in  $Z$ , which can exceed  $10 r_c$  at late times. Fig. 29f) shows how the displacement in  $Z$  depends on the initial orientation of filaments with  $l = 8$ . The filament which obtains the greatest displacement in  $Z$  has  $\theta = 30^\circ$  (simulation *m10c2l8o30* - see Figs. 5-7). It is angled quite steeply to the shock normal and so experiences a good “shove”. The downwards “push” is reduced when  $\theta = 65^\circ$ . Surprisingly, a slight *upwards* push occurs when  $\theta = 85^\circ$ . This is noticeable when  $t \gtrsim 2.5 t_{cs}$ . It appears to be caused by the angle that the shocks transmitted into the sides of the filament move (for example, Fig. 7

shows that in the  $XZ$  plane at  $t = 0.18 t_{cs}$ , the shock transmitted into the “bottom” side of the filament is moving almost directly upwards (to positive  $Z$ ), while its counterpart on the “top” side of the filament is moving at an angle to the  $Z$ -axis).

The mean filament velocity in the direction of shock propagation is shown in Fig. 30a)-c). There is essentially no difference in the asymptotic speed reached, indicating that at late times the filament material has been accelerated up to the speed of the post-shock ambient flow. However, there are differences in the acceleration behaviour of the filament. As indicated previously, side-on filaments accelerate faster than spherical clouds, with longer filaments accelerating the fastest (due to their high surface-to-volume ratio). However, Fig. 30b) shows that all filaments with an initial  $\theta = 30^\circ$  also accelerate faster than spherical clouds. For filaments with  $l = 8$ , Fig. 30c) shows that side-on filaments are accelerated downstream the fastest, while filaments with  $\theta = 60^\circ$  experience the slowest downstream acceleration.

The obliquely-oriented filaments are able to achieve significant velocities perpendicular to the direction of shock propagation, as shown in Fig. 30e)-f). The maximum absolute velocity gained is nearly  $0.1 v_b$  (or about 13% of the postshock flow speed), which occurs in simulation *m10c2l8o30*. However, this is not sustained, and at later times it drops back towards zero. In simulation *m10c2l2o30*, the filament first achieves an overall negative  $Z$ -velocity, before subsequently oscillating first to a positive  $Z$ -velocity and then back to a negative  $Z$ -velocity. This is due to the way in which the cloud fragments (see Fig. 19). Again, we note that the filament in simulation *m10c2l8o85* achieves a slight net positive  $Z$ -velocity.

The interaction of shocks with clouds produces sub-

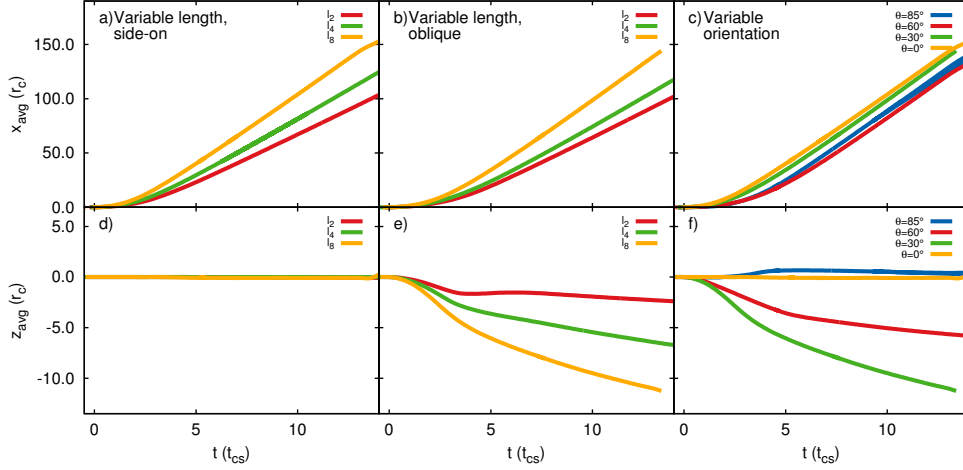


**Figure 29.** The time evolution of the  $X$  and  $Z$  centre-of-mass position of the filament for various simulations (the same simulations as in Fig. 28). The middle panels show simulations with  $\theta = 30^\circ$ . The time is normalized to  $t_{cs}$ .

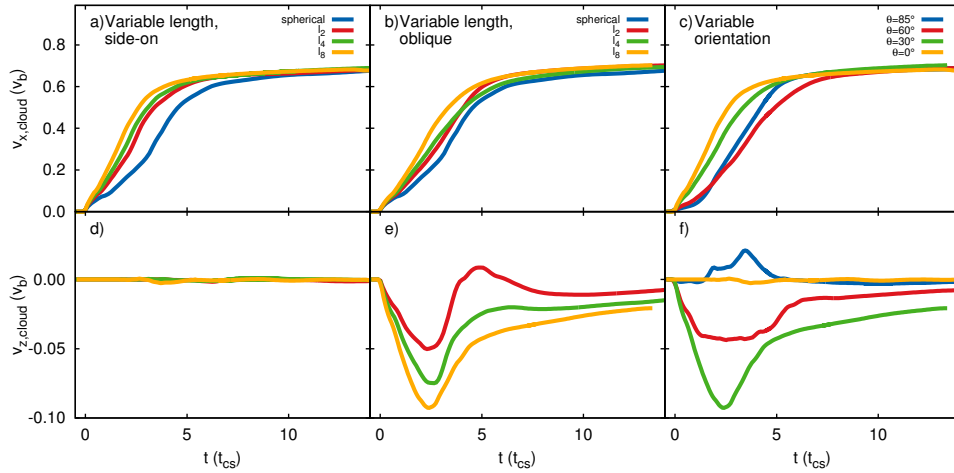


**Figure 30.** As Fig. 29 but showing the time evolution of the filament mean velocity in the direction of shock propagation ( $\langle v_x \rangle_{cloud}$ ) and in the  $Z$ -direction ( $\langle v_z \rangle_{cloud}$ ). The middle panels again show simulations with  $\theta = 30^\circ$ .

stantial vorticity and velocity dispersion, which may be a key mechanism for generating turbulent motions in the ISM (e.g., Kornreich & Scalo 2000; Vázquez-Semadeni et al. 2000; Mac Low & Klessen 2004; Dobbs & Bonnell 2007). From 3D shock-cloud simulations, Nakamura et al. (2006) found that the dependence of the velocity dispersion on region size, the “line width-size” relation, is time-dependent, being approximately flat at early stages in the evolution, but showing a positive trend at later times due to the more rapid damping of small-scale fluctuations. Their one-dimensional velocity dispersions,  $\delta v = \sqrt{(2\delta v_x^2 + \delta v_z^2)/3} \sim 0.1 v_b$ , are consistent with the observed internal motions of about  $1.5 \text{ km s}^{-1}$  observed in cold-neutral-medium (CNM) clouds (Heiles & Troland 2003).

In Fig. 31 we show the filament velocity dispersion in each direction. The most significant finding is that  $\delta v_{x,cloud}$  exceeds  $0.2 v_b$  in some cases (specifically simulations *m10c2l8o60* and *m10c2l8o85*). This is a third higher than for spherical clouds, and for the other filament simulations shown in this plot. It is clearly no coincidence that these two cases correspond to filaments with their long-axis

aligned most closely to the shock normal. It occurs because in these simulations the transmitted shock is still travelling through the filament at the time of this peak in  $\delta v_{x,cloud}$ , and thus there is a large difference in  $v_x$  between different parts of the cloud at this time (see also the MHD simulations of Goldsmith & Pittard 2016). Otherwise, the level of agreement between the various filament simulations is slightly surprisingly -  $\delta v_{x,cloud}$  always peaks at  $\approx 0.15 v_b$ , and  $\delta v_{y,cloud}$  and  $\delta v_{z,cloud}$  peak at  $\approx 0.08 - 0.1 v_b$ . There does not seem to be any significant difference in  $\delta v_{z,cloud}$  with filament orientation, which is unexpected given the clear differences in  $\langle v_z \rangle_{cloud}$  seen in Fig. 30f).

We now examine the dependence of  $m_{core}$ ,  $\langle v_x \rangle_{cloud}$  and  $\langle x \rangle_{cloud}$  on the Mach number and density contrast of a filament with  $l = 8$  and oriented sideways-on to the shock. The Mach number dependence is shown in Fig. 32. As is the case for spherical clouds, we see that  $m_{core}$  decreases more slowly, and  $\langle v_x \rangle_{cloud}$  and  $\langle x \rangle_{cloud}$  both increase more slowly, as  $M$  is reduced.

Fig. 33 shows the dependence of  $m_{core}$ ,  $\langle v_x \rangle_{cloud}$  and  $\langle x \rangle_{cloud}$  as a function of the density contrast,  $\chi$ , for filaments

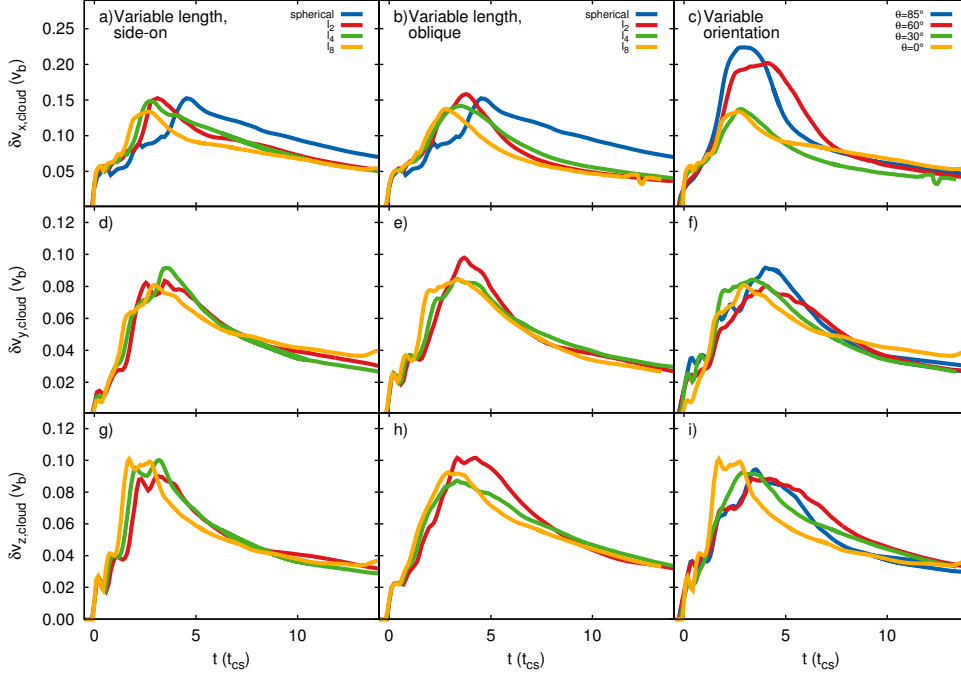


**Figure 31.** As Fig. 29 but showing the time evolution of the filament velocity dispersion in each direction. Panels b), e) and f) show simulations with  $\theta = 30^\circ$ .

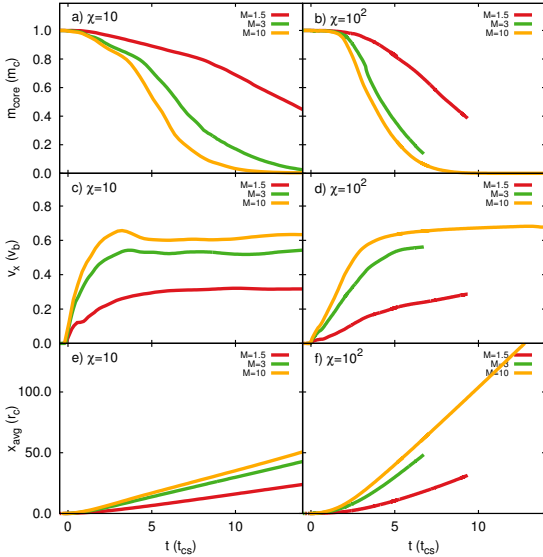


**Figure 32.** The Mach number dependence of the evolution of  $m_{\text{core}}$ ,  $\langle v_x \rangle_{\text{cloud}}$  and  $x_{\text{avg}}$ , for filaments with  $l = 8r_c$  and oriented sideways-on to the shock.

with  $l = 8$  oriented sideways-on to an  $M = 10$  shock. Denser filaments are destroyed relatively quicker, but accelerated relatively slower, when the time is scaled by  $t_{\text{cs}}$ . In contrast, such monotonic behaviour is not seen for spherical clouds - Figs. 14 and 22 and Table 4 in Pittard & Parkin (2016) show that in terms of  $t_{\text{cc}}$ , spherical clouds with  $\chi = 10^2$  are destroyed quicker than clouds with  $\chi = 10^3$ .

### 4.3 Timescales

Values of  $t_{\text{drag}}$  and  $t_{\text{mix}}$  are noted in Table 2. In all cases  $t_{\text{drag}} < t_{\text{mix}}$ . Fig. 34 shows the values of  $t_{\text{drag}}$  and  $t_{\text{mix}}$  from simulations with  $M = 10$  and  $\chi = 10^2$ , as a function of the filament length and orientation. In Fig. 34a) and c), values are plotted from simulations *m10c2l2s*, *m10c2l4s*, and *m10c2l8s* for the “sideways-on” orientation, and from simulations *m10c2l2o30*, *m10c2l4o30*, and *m10c2l8o30* for the “oblique” orientation. In Fig. 34b) and d), values are plotted from simulations *m10c2l8s*, *m10c2l8o30*, *m10c2l8o60* and *m10c2l8o85*. The drag and mixing timescales from a spherical cloud simulation are also plotted in Fig. 34a) and c) as the points at  $l = 0$  (in this case,  $t_{\text{cc}} = t_{\text{cs}}$ ).

Examining Fig. 34a) we see that there is a reduction in the spread between the sideways-on and oblique lines when the time is scaled by  $t_{\text{cs}}$ .  $t_{\text{drag}}$  also shows less variation with length for oblique filaments when scaling to  $t_{\text{cs}}$  ( $t_{\text{drag}}/t_{\text{cc}}$  is surprisingly insensitive to the filament length when the filament is sideways-on). Fig. 34a) also shows that sideways-on filaments have a lower value of  $t_{\text{drag}}$  (i.e. they accelerate faster). Fig. 34b) shows that  $t_{\text{drag}}$  can vary by a factor of 2 or so due to changes in the orientation of the filament.  $t_{\text{drag}}$  increases as the filament orientation moves from sideways-on towards end-on, but the variation is not completely monotonic, with  $t_{\text{drag}}$  declining slightly as the filament becomes nearly end-on. Note that  $t_{\text{cs}} = 1.943 t_{\text{cc}}$  for the results shown in Fig. 34b) and d).

There is also a reduction in the spread between the sideways-on and oblique lines for  $t_{\text{mix}}$  when scaled by  $t_{\text{cs}}$  (see Fig. 34c). In addition, there is much less variation with  $l$  when  $t_{\text{mix}}$  is scaled by  $t_{\text{cs}}$  ( $t_{\text{mix}}/t_{\text{cs}} \approx 4$  for all cases - this further supports our decision to present our results in terms of  $t_{\text{cs}}$ ).  $t_{\text{mix}}$  has the same behaviour with  $\theta$  as  $t_{\text{drag}}$ .

We can compare our results against earlier work from



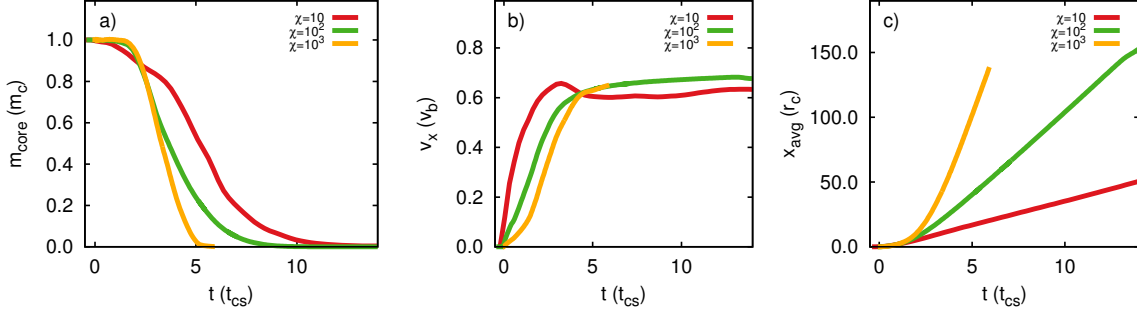


**Figure 33.**  $\chi$  dependence of the evolution, for simulations with  $M = 10$ , and filaments of length  $l = 8 r_c$  oriented sideways on to the shock.

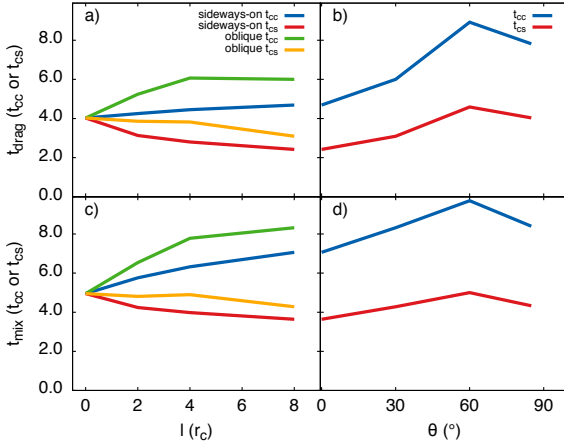


**Figure 34.** Top:  $t_{\text{drag}}$  (for the cloud); and bottom:  $t_{\text{mix}}$ , as functions of the filament length (left panels) and orientation (right panels), from simulations with  $M = 10$  and  $\chi = 10^2$ . The timescales are normalized by either  $t_{cc}$  or  $t_{cs}$ . The “oblique” simulation results noted in the left panels are for  $\theta = 30^\circ$ .

Nakamura et al. (2006), who investigated the interaction of a shock with a soft-edged spherical cloud. These authors also considered the 3D interaction of a shock with a cylindrical cloud, which is effectively an infinite filament hit sideways on (see their Sec. 4.6). They note that cylindrical clouds become more flattened and longer in the transverse direction than spherical clouds (i.e. a larger value of  $a$ ). This increases the drag and leads to more rapid acceleration of the cloud, which in turn results in a longer mixing timescale due to the decreased velocity relative to the surrounding flow. In interactions with  $\chi = 10$  and  $M = 10$ , Nakamura et al. (2006) find that cylindrical clouds with very shallow density gradients ( $n = 2$ ) have  $t_{\text{drag}} = 2.04 t_{cc}$  and  $t_{\text{mix}} = 18.7 t_{cc}$ , which are 0.27 and  $3.95 \times$  their values for a spherical cloud. For clouds with steep density profiles the differences are factors of 0.73 and 1.71 respectively. Our filament has a density profile which is more akin to  $n = 24$  - for the closest comparison we should therefore compare to their  $n = 8$  results. Our nearest equivalent model is simulation *m10c1l8s*. In terms of  $t_{cc}$ , we find that  $t_{\text{drag}}$  ( $t_{\text{mix}}$ ) is 53% (146%) of the values for a spherical cloud for simulation *m10c1l8s*. These factors are both smaller than the factors found by Nakamura et al.

(2006), but are in reasonable agreement considering that our filaments have slightly sharper density profiles and are finite in extent (note also that  $t_{\text{mix}}$  increases as the filament length increases). For interactions with filaments of higher density contrast (specifically  $\chi = 10^2$ , simulation *m10c2l8s*), we find that  $t_{\text{drag}}$  increases by a factor of 1.17 (see Fig. 34a), while  $t_{\text{mix}}$  increases by a factor of 1.43 (see Fig. 34c).

The characteristic drag time can be obtained from the equation of motion of the cloud,

$$m_c \frac{dv'_c}{dt} = -\frac{1}{2} C_D \rho_{i1} v'^2_c A, \quad (13)$$

where  $m_c$  is the mass of the cloud,  $v'_c = |v_{i1} - v_c|$  is the magnitude of the velocity of the cloud ( $v_c$ ) relative to the shocked intercloud medium ( $v_{i1}$ ),  $C_D$  is the drag coefficient,  $\rho_{i1}$  is the density of the shocked intercloud medium, and  $A$  is the cross-sectional area of the cloud normal to the shock normal (see, e.g., Klein et al. 1994). The cloud accelerates so that  $v'_c = v_{i1}/e$  at the time

$$t_{\text{drag}} = \frac{2m_c}{C_D \rho_{i1} A} \frac{(e-1)}{v_{i1}}. \quad (14)$$

For a strong shock and  $\gamma = 5/3$ ,  $\rho_{i1} \approx 4\rho_{i0}$ , where  $\rho_{i0}$  is the density of the preshock ambient medium. Then for a spherical cloud, with  $m_c = \frac{4}{3}\pi r_c^3 \rho_{i0} \chi$  and  $A = \pi r_c^2$ ,  $v'_c = v_{i1}/e$  when  $t_{\text{drag}} = 1.53 \chi^{1/2} t_{cc}/C_D$ . Of course, the lateral expansion of the cloud increases  $A$ , so the actual drag time is considerably smaller. Alternatively, one can keep the original value of  $A$  and instead account for this expansion with a larger value of  $C_D$ .

For a filament with mass  $m_c = (l + \frac{4}{3})\pi r_c^3 \rho_{i0} \chi$  and cross-sectional area  $A = (l \cos \theta + \pi) r_c^2$  (where  $\theta$  is the angle between the filament long axis and the shock surface),

$$t_{\text{drag}} = 3.60 \frac{(l + 4/3)}{(l \cos \theta + \pi)} \frac{\chi^{1/2}}{C_D} t_{cc} = 3.96 \frac{(l + 4/3)^{2/3}}{(l \cos \theta + \pi) C_D} t_{cs}. \quad (15)$$

For a very long filament sideways-on to the shock ( $\theta = 0^\circ$ ),  $t_{\text{drag}} \propto l^{-1/3}$ . For very long filaments end-on to the shock ( $\theta = 90^\circ$ ),  $t_{\text{drag}} \propto l^{2/3}$ .

Fig. 35 shows the values of  $t_{\text{drag}}$  from simulations with  $M = 10$  and  $\chi = 10^2$  compared to the analytical value from Eq. 15. We immediately see that the simulation values do not follow the same trend with  $l$  or  $\theta$  as the simple analytical theory. In particular, we note that  $t_{\text{drag}}$  peaks at  $\theta \sim 60^\circ$  in the simulations, whereas the analytical theory predicts that  $t_{\text{drag}}$  peaks at  $\theta = 90^\circ$  (i.e. end-on). This indicates that the real behaviour of the filament is more complex. For

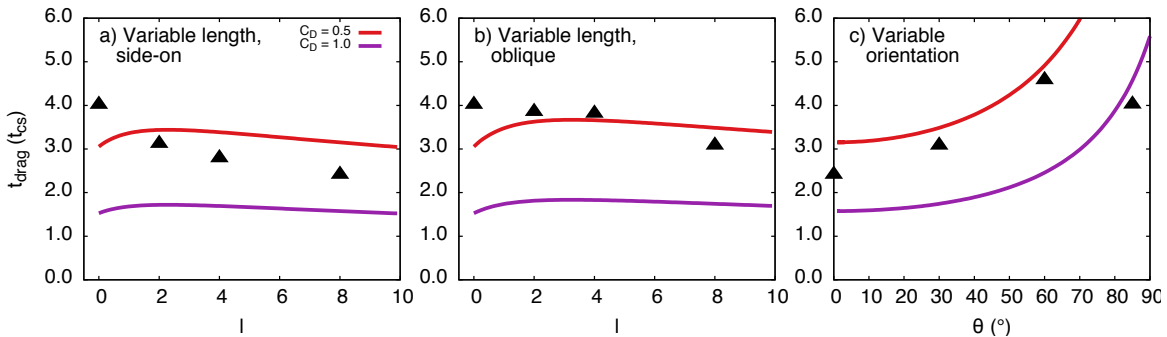


**Figure 35.**  $t_{\text{drag}}$  from the simulations compared to the analytical expression in Eq. 15, for  $M = 10$  and  $\chi = 10^2$ . a) As a function of filament length, for side-on filaments. b) As a function of filament length for oblique filaments ( $\theta = 30^\circ$ ). c) As a function of orientation for filaments of length  $l = 8$ . The filament is sideways-on when  $\theta = 0^\circ$  and is end-on when  $\theta = 90^\circ$ .

instance, its lateral expansion is likely a function of its length and orientation, while its acceleration is also driven by the transmitted shocks and rarefaction waves.

For sideways-on finite *rigid* cylinders,  $C_D$  decreases as the aspect ratio ( $L/D$ ) of the cylinder decreases (see, e.g., Baban & So 1991, and references therein).  $C_D \sim 1$  for sub-critical, high Reynolds numbers, but is significantly higher at lower  $Re$  (e.g., at  $Re = 1$ ,  $C_D \approx 20$  for  $L/D = 2$ , and declines to  $C_D = 12$  at  $L/D = 20$ , as shown in Vakil & Green 2009). A decline in  $C_D$  with  $L/D$  is equivalent to  $t_{\text{drag}}$  increasing as  $l$  decreases. This is indeed the behaviour found in our numerical simulations as shown in Fig. 35a-b). Vakil & Green (2009) also show that the drag coefficient increases as the cylinder moves from end-on to side-on, while the lift coefficient is a maximum at  $\theta \approx 45^\circ$ . The fact that  $C_D$  monotonically decreases as the cylinder rotates to become more end-on is equivalent to  $t_{\text{drag}}$  monotonically increasing with  $\theta$ . This is of course the behaviour obtained with Eq. 15, but as already noted our simulation results do not yield such monotonic behaviour for  $t_{\text{drag}}$  (see Fig. 35c). The ratio of the lift-to-drag coefficients,  $C_L/C_D$ , peaks at  $\theta \approx 50^\circ$ . For  $Re = 40$ ,  $C_L/C_D = 0.3$  (0.17) at  $L/D = 5$  (2) (Vakil & Green 2009). It is interesting to note that the ratio of the peak values of the average cloud velocities normal to and with the flow in simulation *m10c2l8o30* is  $\approx 0.15$  (see Fig. 30).

The values of  $t_{\text{drag}}$  and  $t_{\text{mix}}$  are very relevant to the acceleration and survival of clouds in multi-phase galactic winds. Recent observations indicate that the cool gas extends to large distances from the host galaxy, up to the virial radius (e.g., Ribaudo et al. 2011; Rudie et al. 2012; Crighton, Hennawi & Prochaska 2013; Werk et al. 2014). However, it is not clear whether clouds can be accelerated by the ram pressure of the hot wind to the observed distances and velocities. For instance, Scannapieco & Brüggen (2015) find that clouds are completely disrupted by their interaction with a wind by the time they travel  $40r_c$ , and that it is therefore very difficult to explain the 100 kpc distances at which cool gas is seen from nearby galaxies. They also find that clouds are accelerated to only very small fractions ( $\lesssim 0.3$ ) of the wind speed. On the other hand, McCourt et al. (2015) find that mixing is suppressed for clouds with tangled internal

magnetic fields<sup>3</sup>, such that they *can* be accelerated up to the wind speed. Taking the lifetime of clouds as  $\approx 10t_{\text{cc}}$ , in agreement with the results from shock-cloud simulations (e.g., see Fig. 19 in Pittard et al. 2010), Zhang et al. (2015) estimate that the KH timescale must be roughly  $3 - 10\times$  longer than that from purely hydrodynamic simulations in order for cool clouds to reach the velocities seen in observations.

An obvious question is whether filaments as opposed to spherical clouds can alleviate some of these issues. The current paper indicates that  $t_{\text{drag}}/t_{\text{cc}}$  varies little with filament length, and that side-on or nearly-side on filaments accelerate at approximately the same rate as spherical clouds ( $t_{\text{drag}}/t_{\text{cc}}$  is within  $\pm 50\%$ ). For longish filaments oriented nearly end-on ( $l = 8, \theta = 60^\circ$ ),  $t_{\text{drag}}$  can be a factor of 2 longer. But as  $t_{\text{mix}}/t_{\text{cc}}$  is only 40% longer, they do not travel as far downstream by  $t = t_{\text{mix}}$ . Nakamura et al. (2006) report that  $t_{\text{mix}}/t_{\text{drag}}$  remains almost constant for clouds with very smooth density profiles (see their Tables 1 and 2).

The average displacement of the filament in the downstream direction  $\langle x \rangle$  at  $t = t_{\text{mix}}$  is noted in Table 2. Some trends are worth noting. Firstly,  $\langle x \rangle/r_c$  roughly decreases with increasing  $\theta$  (e.g., from a value of 21.2 for simulation *m10c2l8s* to 11.9 for simulation *m10c2l8o85*). Second,  $\langle x \rangle/r_c$  increases with  $l$  for sideways-on filaments (e.g., from 14.8 for *m10c2l2s* to 21.2 for *m10c2l8s*), and also increases with  $\chi$  for  $M = 10$ ,  $l = 8$ , sideways-on filaments (from 17.6 for *m10c1l8s* to 28.6 for *m10c3l8s*).

In fact, Table 2 indicates that simulation *m10c3l8s* has the highest value of  $\langle x \rangle/r_c$  ( $= 28.6$ ) at  $t = t_{\text{mix}}$  ( $= 6.46t_{\text{cc}}$  for this simulation). This filament travels nearly as far as the furthest distance reported by Scannapieco & Brüggen (2015), where  $d = 32r_c$  for their simulation *M11.4v3000* ( $\chi = 300$ ) at  $t = t_{25}$  (defined as the time when only 33% of the cloud mass is at or above the original density, which corresponds to  $t = 22.2t_{\text{cc}}$  in this simulation). However, the velocity of the cloud material differs markedly between our work and theirs. The core material in our simulation has  $\langle v_x \rangle/v_b = 0.40$  whereas in their simulation their cloud has only reached a velocity of  $v = 0.14v_{\text{hot}}$  ( $420 \text{ km s}^{-1}$ ). At face level our results would seem to be more favourable compared

<sup>3</sup> This is also the case for magnetized shocks interacting with filaments (Goldsmith & Pittard 2016).



to observations of galactic winds. However, it is hard to make a more direct comparison because of the different tracers used for the cloud ( $m_{\text{core}}$  in our work versus  $F_{1/3}$  in their work), and a dedicated study is needed to investigate this issue further.

## 5 SUMMARY AND CONCLUSIONS

In this paper we have investigated the hydrodynamic interaction of a shock with a filament. This extends previous investigations of a shock striking a spherical cloud (e.g., Stone & Norman 1992; Klein et al. 1994; Nakamura et al. 2006; Pittard & Parkin 2016) to interactions with highly elongated clouds. Two additional parameters are introduced: the length of the filament ( $l$ ) and its orientation to the shock ( $\theta$ ). We have performed 3D simulations in which these parameters are varied, with our main focus on a Mach 10 shock interacting with a  $\chi = 10^2$  filament. Our main conclusions are as follows:

(i) We find significant differences in the interaction as  $l$  and  $\theta$  are varied. In particular, we find that filaments with  $l \gtrsim 2r_c$  which are oriented at  $\theta \lesssim 60^\circ$  form 3 parallel rolls during the interaction, which move away from each other as the filament material mixes into the ambient flow. In sideways-on filaments, the filament material expands preferentially along its minor-axis and in the direction of shock propagation, and much less so along its major-axis.

(ii) The nature of the interaction changes significantly with the initial obliquity of the filament. Filaments oriented only slightly oblique to the shock surface (at  $\theta = 30^\circ$ ) spill flow with high vorticity around the upstream end of the filament, while periodic vortex shedding occurs at the downstream end. Their wakes are longer and less symmetrical. Increasing the obliquity further ( $\theta = 60^\circ$ ) suppresses the 3-parallel rolls - instead the vortex ring which forms at the upstream end of the filament is the dominant flow feature and is the cause of the filament's fragmentation. Filaments which are almost end-on to the shock ( $\theta = 85^\circ$ ) suffer dramatic "hollowing" or "voiding", followed by strong instabilities at their upstream end. Destruction occurs by the time that the transmitted shock reaches the back of the filament.

(iii) Sideways-on filaments initially lose mass more quickly, but since they are also accelerated more quickly the final 20% of their mass loss occurs more gradually. Filaments oriented at an angle of  $60^\circ$  to the shock front lose mass more slowly than those at other orientations. Even a small elongation from spherical can significantly change the destruction timescale.

(iv) The rate at which the filaments lose mass shows less variance between different simulations when the time is normalized in terms of  $t_{\text{cs}}$ , the "cloud crushing time" for a spherical cloud of the same density contrast and equivalent mass. When normalized in terms of  $t_{\text{cs}}$ , side-on filaments are destroyed more quickly than spherical clouds due to their greater surface area to volume ratio.

(v) Filaments which are oriented at an angle to the shock can obtain velocities of order 10% of the shock speed in directions perpendicular to the shock normal, for short periods of time. Filaments which are closely aligned with the shock normal can actually be pushed in a different transverse direction than expected.

(vi) The filament velocity dispersion varies very little with length or orientation, except for filaments with  $l = 8r_c$  which have their long-axis within  $30^\circ$  of the shock normal. There does not seem to be any significant difference in  $\delta v_{z,\text{cloud}}$  with filament orientation, despite clear differences in  $\langle v_z \rangle_{\text{cloud}}$ .

(vii) Sideways-on filaments have a lower value of  $t_{\text{drag}}$  (i.e. they accelerate faster).  $t_{\text{drag}}$  can vary by a factor of 2 or so due to changes in the orientation of the filament:  $t_{\text{drag}}$  increases as the filament orientation moves from sideways-on towards end-on, but the variation is not completely monotonic, and there is a slight reduction as the filament becomes nearly end-on.  $t_{\text{mix}}$  shows similar behaviour.

(viii) The nature of the interaction mirrors that of spherical cloud interactions as  $M$  and  $\chi$  are varied. The interaction is much less violent at lower Mach numbers, and both  $t_{\text{drag}}/t_{\text{cs}}$  and  $t_{\text{mix}}/t_{\text{cs}}$  increase. Filaments with a lower density contrast are less able to resist the shock and their immersion in the post-shock flow, and are rapidly accelerated towards the postshock speed. Filaments with a higher density contrast are accelerated more slowly and are subject to stronger instabilities.

In a companion paper (Goldsmith & Pittard 2016) we examine the effect of a magnetic field on shock-filament interactions, and in future work we will explore the effects of additional physics, such as radiative cooling, and the interaction with a wind rather than a shock.

## ACKNOWLEDGEMENTS

We would like to thank the referee for a timely and useful report. JMP would like to thank S. Falle for the use of the MG hydrodynamics code used to calculate the simulations in this work and S. van Loo for adding SILO output to it. This work was supported by the Science & Technology Facilities Council [Research Grant ST/L000628/1]. The calculations for this paper were performed on the DiRAC Facility jointly funded by STFC, the Large Facilities Capital Fund of BIS and the University of Leeds.

## REFERENCES

- Agertz O., et al., 2007, MNRAS, 380, 963
- André Ph., et al., 2010, A&A, 518, L102
- Arthur, S. J., & Henney, W. J. 1996, ApJ, 457, 752
- Arzoumanian D., et al., 2011, A&A, 529, L6
- Baban F., So R. M. C., 1991, Experiments in Fluids, 10, 313
- Ballesteros-Paredes J., Mac Low M.-M., 2002, ApJ, 570, 734
- Bate M. R., Bonnell I. A., 2005, MNRAS, 356, 1201
- Benjamin R. A., et al., 2003, PASP, 115, 953
- Beuther H., et al., 2011, A&A, 533, A17
- Bolatto A. D., et al., 2013, Nature, 499, 450
- Bonnell I. A., Dobbs C. L., Smith R. J., 2013, MNRAS, 430, 1790
- Bruhweiler F. C., Ferrero R. F., Bourdin M. O., Gull T. R., 2010, ApJ, 719, 1872
- Canning R. E. A., Fabian A. C., Johnstone R. M., Sanders

- J. S., Crawford C. S., Ferland G. J., Hatch N. A., 2011, MNRAS, 417, 3080
- Carey S. J., et al., 2009, PASP, 121, 76
- Cecil G., Bland-Hawthorn J., Veilleux S., Filippenko A. V., 2001, ApJ, 555, 338
- Chièze, J. P., & Lazareff, B. 1981, A&A, 95, 194
- Churchwell E., et al., 2009, PASP, 121, 213
- Close, J., Pittard, J. M., Hartquist, T. W., & Falle, S. A. E. G., 2013, MNRAS, 436, 3021
- Colín P., Vázquez-Semadeni E., Gómez G. C., 2013, MNRAS, 435, 1701
- Conselice C. J., Gallagher III J. S., Wyse R. F. G., 2001, AJ, 122, 2281
- Cooper J. L., Bicknell G. V., Sutherland R. S., Bland-Hawthorn J., 2008, ApJ, 674, 157
- Cowie, L. L., McKee, C. F., & Ostriker, J. P. 1981, ApJ, 247, 908
- Crawford C. S., Hatch N. A., Fabian A. C., Sanders J. S., 2005, MNRAS, 363, 216
- Crighton N. H. M., Hennawi J. F., Prochaska J. X., 2013, ApJ, 776, L18
- Dale J. E., Bonnell I. A., 2011, MNRAS, 414, 321
- Davidson P. A., 2004, “Turbulence. An Introduction for Scientists and Engineers”, Oxford University Press
- Dent W. R. F., et al., 2009, MNRAS, 395, 1805
- Dobbs C. L., Bonnell I. A., 2007, MNRAS, 374, 1115
- Dursi L. J., Pfrommer C., 2008, ApJ, 677, 993
- Dyson, J. E., Arthur, S. J., & Hartquist, T. W. 2002, A&A, 390, 1063
- Dyson, J. E., & Hartquist, T. W. 1987, MNRAS, 228, 453
- Elmegreen B. G., Scalo J., 2004, ARA&A, 42, 211
- Engelbracht C. W., et al., 2006, ApJ, 642, L127
- Falle S. A. E. G., 1991, MNRAS, 250, 581
- Farris M. H., Russell C. T., 1994, J. Geophys. Research, 99, 17681
- Federrath C., Roman-Duval J., Klessen R. S., Schmidt W., Mac Low M.-M., 2010, A&A, 512, A81
- Fernández-López M., et al., 2014, ApJ, 790, L19
- Forman W., et al., 2007, ApJ, 665, 1057
- Fröhlich J., Rodi W., 2004, Int. Journ. Heat and Fluid Flow, 25, 537
- Fujita A., Martin C. L., Mac Low M.-M., New K. C. B., Weaver R., 2009, ApJ, 698, 693
- Gaspari M., Ruszkowski M., Sharma P., 2012, ApJ, 746, 94
- Georgievskiy P. Yu., Levin V. A., Sutyryn O. G., 2015, Shock Waves, 25, 357
- Glover S. C. O., Clark P. C., 2012, MNRAS, 426, 377
- Goldsmith K. J. A., Pittard J. M., 2016, MNRAS, submitted
- Goodman A. A., et al., 2014, ApJ, 797, 53
- Gómez G. C., Vázquez-Semadeni E., 2014, ApJ, 791, 124
- Gregori G., Miniati F., Ryu D., Jones T. W., 2000, ApJ, 543, 775
- Hacar A., Tafalla M., Kauffmann J., Kovács A., 2013, A&A, 554, A55
- Heeson V., Beck R., Krause M., Dettmar R.-J., 2011, A&A, 535, A79
- Heiles C., Troland T. H., 2003, ApJ, 586, 1067
- Heitsch F., Hartmann L., 2008, ApJ, 689, 290
- Hennebelle P., 2013, A&A, 556, A153
- Hennemann M., et al., 2012, A&A, 543, L3
- Henning Th., et al., 2010, A&A, 518, L95
- Henshaw J. D., Caselli P., Fontani F., Jiménez-Serra I., Tan J. C., 2014, MNRAS, 440, 2860
- Hoopes C. G., et al., 2005, ApJ, 619, L99
- Jackson J. M., et al., 2010, ApJ, 719, L185
- Johansson E. P. G., Ziegler U., 2013, ApJ, 766, 45
- Juvela M., et al., 2012, A&A, 541, A12
- Kappler M., 2002, Ph.D. thesis, Institute for Hydromechanics, University of Karlsruhe
- Kawamura T., Hiwada M., Hibino T., Mabuchi I., Kamuda M., 1984, “Flow around a finite circular cylinder on a flat plate”, Bull. JSME 27 (232), 2142
- Kirk H., Klassen M., Pudritz R., Pillsworth S., 2015, ApJ, 802, 75
- Klein R. I., McKee C. F., Colella P., 1994, ApJ, 420, 213
- Klein R. I., Budil K. S., Perry T. S., Bach D. R., 2003, ApJ, 583, 245
- Klessen R. S., Burkert A., 2000, ApJS, 128, 827
- Kornreich P., Scalo J., 2000, ApJ, 531, 366
- Krumholz M. R., Klein R. I., McKee C. F., 2011, ApJ, 740, 74
- Larose G. L., Savage M. G., Jakobsen J. B., 2003, Wind tunnel experiments on an inclined and yawed circular cylinder in the critical Reynolds number range, in Proceedings of the Eleventh International Conference on Wind Engineering, Lubbock, TX, p. 1705
- Leaõ M. R. M., de Gouveia Dal Pino E. M., Falceta-Gonçalves D., Melioli C., Geraissate F. G., 2009, MNRAS, 394, 157
- Li S., Frank A., Blackman E. G., 2013, ApJ, 774, 133
- Li Z.-Y., Wang P., Abel T., Nakamura F., 2010, ApJ, 720, L26
- Mac Low M.-M., Klessen R., 2004, Rev. Mod. Phys., 76, 125
- Martin C. L., Kobulnicky H. A., Heckman T. M., 2002, ApJ, 574, 663
- Matsumoto M., Shiraishi N., Kitazawa M., Knisely C., Shirato H., Kim Y., Tsujii M., 1990, J. Wind Eng. Ind. Aerodyn., 33, 63
- McCourt M., O’Leary R. M., Madigan A.-M., Quataert E., 2015, MNRAS, 449, 2
- McDonald M., Veilleux S., Rupke D. S. N., Mushotzky R., 2010, ApJ, 721, 1262
- McKee, C. F., & Ostriker, J. P. 1977, ApJ, 218, 148
- Menshchikov A., et al., 2010, A&A, 518, L103
- Moeckel N., Burkert A., 2015, ApJ, 807, 67
- Molinari S., et al., 2010, A&A, 518, L100
- Motte F., et al., 2010, A&A, 518, L77
- Nakamura F., McKee C. F., Klein R. I., Fisher R. T., 2006, ApJSS, 164, 477
- Niederhaus J. H. J., 2007, PhD thesis, University of Wisconsin - Madison
- Niederhaus J. H. J., Greenough J. A., Oakley J. G., Ranjan D., Anderson M. H., Bonazza R., 2008, J. Fluid Mech., 594, 85
- Ntormousi E., Burkert A., Fierlinger K., Heitsch F., 2011, ApJ, 731, 13
- Ohya Y., et al., 2002, PASJ, 54, 891
- Okamoto T., Yagita M., 1973, Bull. JSME, 95, 805
- Orlando S., Peres G., Reale F., Bocchino F., Rosner R., Plewa T., Siegel A., 2005, A&A, 444, 505
- Padoan P., et al., 2001, ApJ, 553, 227
- Padoan P., Cambrésy L., Juvela M., Kritsuk A., Langer

W. D., Norman M. L., 2006, *ApJ*, 649, 807

Palmeirim P., et al., 2013, *A&A*, 550, A38

Park C.-W., Lee S.-J., 2000, *Journal Wind Engineering and Industrial Aerodynamics*, 88, 231

Peretto N., et al., 2012, *A&A*, 541, A63

Pittard, J. M., Arthur, S. J., Dyson, J. E., Falle, S. A. E. G., Hartquist, T. W., Knight M. I., & Pexton M. 2003, *A&A*, 401, 1027

Pittard J. M., Falle S. A. E. G., Hartquist T. W., Dyson J. E., 2009, *MNRAS*, 394, 1351

Pittard J. M., Hartquist T. W., Falle S. A. E. G., 2010, *MNRAS*, 405, 821

Pittard J. M., Parkin E. R., 2016, *MNRAS*, accepted

Porter D., et al., 1994, *Phys. Fluids*, 6, 2133

Raga A. C., Esquivel A., Riera A., Velázquez P. F., 2007, *ApJ*, 668, 310

Ramberg S. E., 1983, *J. Fluid Mech.*, 128, 81

Ribaudo J., Lehner N., Howk J. C., Werk J. K., Tripp T. M., Prochaska J. X., Meiring J. D., Tumlinson J., 2011, *ApJ*, 743, 207

Rich J. A., Dopita M. A., Kewley L. J., Rupke D. S. N., 2010, *ApJ*, 721, 505

Rodríguez-González A., Esquivel A., Raga A. C., Cantó J., 2008, *ApJ*, 684, 1384

Rogers H., Pittard J. M., 2013, *MNRAS*, 431, 1337

Rudie G. C., et al., 2012, *ApJ*, 750, 67

Sales L. V., Navarro J. F., Schaye J., Dalla Vecchia C., Springel V., Booth C. M., 2010, *MNRAS*, 409, 1541

Scalo J., Elmegreen B. G., 2004, *ARA&A*, 42, 275

Scannapieco E., Brüggemann M., 2015, *ApJ*, 805, 158

Schneider N., et al., 2006, *A&A*, 458, 855

Schneider S., Elmegreen B. G., 1979, *ApJS*, 41, 87

Seifried D., Walch S., 2015, *MNRAS*, 452, 2410

Sharp R. G., Bland-Hawthorn J., 2010, *ApJ*, 711, 818

Shin M.-S., Stone J. M., Snyder G. F., 2008, *ApJ*, 680, 336

Shirakashi M., Hasegawa A., Wakiya S., 1986, *Bull. Jpn. Soc. Mech. Eng.* 29, 250, 1124

Shopbell P. L., Bland-Hawthorn J., 1998, *ApJ*, 493, 129

Smith R. J., Glover S. C. O., Klessen R. S., 2014, *MNRAS*, 445, 2900

Stone J. M., Norman M. L., 1992, *ApJ*, 390, L17

Strickland D. K., Stevens I. R., 2000, *MNRAS*, 314, 511

Strickland D. K., Heckman T. M., Colbert E. J. M., Hoopes C. G., Weaver K. A., 2004, *ApJSS*, 151, 193

Vaidya B., Hartquist T. W., Falle S. A. E. G., 2013, *MNRAS*, 433, 1258

Vakil A., Green S. I., 2009, *Computers & Fluids*, 38, 1771

Van Loo S., Falle S. A. E. G., Hartquist T. W., 2010, *MNRAS*, 406, 1260

Vázquez-Semadeni E., 1994, *ApJ*, 423, 681

Vázquez-Semadeni E., Ostriker E. C., Passot T., Gammie C. F., Stone J. M., 2000, in *Protostars and Planets IV*, ed. V. Mannings, A. P. Boss & S. S. Russell (Tucson: Univ. Arizona Press), 3

Vázquez-Semadeni E., Ryu D., Passot T., González R. F., Gazol A., 2006, *ApJ*, 643, 245

Vázquez-Semadeni E., et al., 2010, *ApJ*, 715, 1302

Veilleux S., Rupke D. S. N., 2002, *ApJ*, 565, L63

Veilleux S., Cecil G., Bland-Hawthorn J., 2005, *ARA&A*, 43, 769

Vig S., Testi L., Walmsley M., Molinari S., Carey S., Noriega-Crespo A., 2007, *A&A*, 470, 977

Werk J. K., et al., 2014, *ApJ*, 792, 8

Westmoquette M. S., Smith L. J., Gallagher III J. S., 2011, *MNRAS*, 414, 3719

White, R. L., & Long, K. S. 1991, *ApJ*, 373, 543

Williamson C. H. K., 1996, *Annu. Rev. Fluid Mech.*, 28, 477

Wilson B. A., Dame T. M., Mashedier M. R. W., Thaddeus P., 2005, *A&A*, 430, 523

Xu J., Stone J. M., 1995, *ApJ*, 454, 172

Yeo D., Jones N. P., 2008, *J. Wind Eng. Ind. Aerodyn.*, 96, 1947

Yirak K., Frank A., Cunningham A., 2010, *ApJ*, 722, 412

Zdravkovich M. M., 2003, *Flow Around Circular Cylinders*, Vol. 2: Applications, Oxford University Press

Zhang D., Thompson T. A., Quataert E., Murray N., 2015, arXiv:1507.01951

## APPENDIX A: RESOLUTION TEST

The damping of hydromagnetic waves, through either particle collisions or wave-particle interactions, sets the length scale,  $\eta$ , of the smallest instabilities in the actual interaction of a shock with an obstacle (see the discussion in Pittard et al. 2009). The Reynolds number of the interaction is given by  $Re = (l/\eta)^{4/3}$ , where  $l$  is the characteristic size of the largest eddies (typically the size of the obstacle). In astrophysical settings,  $Re$  can easily exceed  $10^5 - 10^6$ . At such high values, the flow will develop turbulent-like characteristics (i.e., rapid variations in the fluid properties in time and space). Resolving the smallest eddies in a numerical simulation can be very challenging, which is why some studies make use of subgrid turbulent viscosity models (e.g., the  $k-\epsilon$  model) which add turbulent-specific viscosity and diffusion terms to the Euler equations (e.g., Pittard et al. 2009, 2010; Pittard & Parkin 2016).

For simulations which simply solve the Euler equations for inviscid fluid flow, new unstable scales will be added as the resolution of the simulation is increased, since there is no prescription for small-scale dissipative physics. In such “inviscid” simulations, the nature of the interaction of a shock with an obstacle will depend on the resolution used. At higher resolution, smaller instabilities can develop and features in the flow (e.g., shocks and interfaces) become sharper. The effective or grid-scale Reynolds number of the flow is  $Re = (l/\eta)^{4/3}$ , where  $\eta$  is now the minimum eddy size in the simulation ( $\eta \approx 2\Delta x$ , where  $\Delta x$  is the grid cell size). Hence, calculations at lower resolution effectively simulate a more viscous flow. In shock-cloud simulations, this can affect the rate at which material is stripped from the cloud and mixed into the post-shock flow, and the acceleration of the cloud. Important features of the flow may not be present at very low resolution, and the simulated interaction will compare poorly to reality.

Simulations of problems for which there is no analytical solution typically rely on a demonstration of self-convergence. However, care must be taken to avoid “false convergence” (e.g., Niederhaus 2007). Formal convergence may be impossible in “inviscid” simulations - where convergence is demonstrated, it may only apply to specific global quantities, and at the earlier stages of the interaction. Rather than attempting to demonstrate formal convergence,

some previous studies have instead focussed on resolving key features in the flow. In shock-cloud simulations this could include the stand-off distance of the bowshock (e.g., Farris & Russell 1994), the thickness of the turbulent boundary layer (e.g., Pittard et al. 2009), the cooling layer behind shocks (Yirak et al. 2010), and the magnetic draping layer in magnetized interactions (Dursi & Pfrommer 2008).

A resolution test for 3D adiabatic shock-cloud simulations was performed by Pittard & Parkin (2016). It was found that 32–64 cells per cloud radius were needed to capture the main flow features and for reasonable convergence of some key global quantities. Here we examine how shock-filament interactions are affected by the resolution used.

### A1 Filament morphology

Fig. A1 shows the effect of the resolution on the interaction in simulation *m10c2l8s*, at  $t = 1.58 t_{cs}$ . The filament is oriented side-on to the shock, and we view it from one end in the top row of panels, and face-on in the bottom row of panels. As the resolution increases the shape of the cloud changes, from smooth and relatively featureless, to displaying 2 and then 3 parallel rolls at the two highest resolutions. The downstream wake shows characteristics of turbulence at resolution  $R_{32}$ . Fig. A2 shows equivalent snapshots at the slightly later time of  $t = 2.28 t_{cs}$ . The filament in the lowest resolution simulation has moved slightly further downstream than the others. The shape of the rolls is slightly different between simulations at  $R_{16}$  and  $R_{32}$ , but generally speaking the  $R_{16}$  simulation appears to have captured the main features of the interaction. Additional smaller-scale structure is present at  $R_{32}$ .

Fig. A3 shows the effect of the grid resolution on simulation *m10c2l8o60*. Here the filament is oriented at an angle of  $30^\circ$  to the shock normal. Here the broad features of the flow are present even at  $R_4$ , but increasing resolution shows the up-stream tip of the filament becoming more and more hollow as an asymmetric vortex roll forms around it. Material at the up-stream tip is thus ripped off the filament in this way.

Figs. A4 and A5 show the effect of the grid resolution on two simulations where the filament is significantly shorter (models *m10c2l2s* and *m10c2l2o30*, respectively). Fig. A4 also shows that the cloud forms first 2, and then 3 parallel rolls as the resolution increases from  $R_8$  to  $R_{16}$  and  $R_{32}$ . However, increasing the resolution further to  $R_{64}$  shows that the prominence of the rolls reduces slightly as additional non-axisymmetric structure forms. In Fig. A5 we see the same hollowing of the filament tip seen for longer filaments (cf. Fig. A3). In this case the  $R_{64}$  simulation shows additional structure but also largely maintains the general features seen at  $R_{32}$ .

In summary, one obtains the general impression that  $R_{16}$  often captures the main morphological features of the interaction, but that  $R_{32}$  is really the minimum needed for a more accurate description of the flow. This requirement is maybe a little below that for spherical clouds, where  $\sim R_{64}$  is identified as the minimum necessary resolution in purely hydrodynamical interactions (Xu & Stone 1995; Pittard & Parkin 2016). However, the lower resolution requirement for filaments compared to spherical clouds is perhaps not too unexpected given that we measure the resolution across the

short axis of the filament. To compare more fairly, we could instead consider the respective volumes of the filament and the spherical cloud. The volume of the filament in model *m10c2l8s* is  $7\times$  that of a spherical cloud of equivalent cross-section. A spherical cloud with the same volume as this filament would thus have a radius  $1.91\times$  larger. Hence the *effective* resolution of an  $R_{32}$  simulation of model *m10c2l8s* could be argued to be  $R_{61}$ .

### A2 Time Evolution

Fig. A6 shows the time evolution of the core mass,  $m_{core}$ , and the mean filament speed,  $\langle v_{x,cloud} \rangle$ , for a number of simulations where the filament length  $l = 8 r_c$ . In all cases we observe good convergence, with only the  $R_4$  resolution simulations showing significant divergence from the others. Closer examination reveals that there is less difference between the  $R_{16}$  and  $R_{32}$  simulations, than between the  $R_8$  and  $R_{16}$  simulations, consistent with convergence.

The only other resolution test for non-spherical clouds which we are aware of in the literature is in Xu & Stone (1995), where prolate clouds with an axial ratio of 2:1 and  $\chi = 10$  are struck by a Mach 10 shock. Their Fig. 8 shows the resolution dependence of the time evolution of various global properties of the cloud when it is initially oriented with its long-axis perpendicular to the shock normal (i.e. sideways on). The mean cloud speed is very insensitive to the range of resolutions considered (corresponding to  $R_7$ ,  $R_{16}$ , and  $R_{32}$  in our terminology), though the mixing fraction,  $f_{mix}$  is significantly different at  $R_7$ . Our results for longer and denser filaments are roughly consistent with their findings.

In their Fig. 10, Xu & Stone (1995) show similar plots for an inclined cloud (with the semi-major axis at  $45^\circ$  to the shock normal). Only  $R_7$  and  $R_{14}$  calculations are compared – again the mean cloud velocity is very insensitive to the resolutions examined, but there are some more significant differences for  $f_{mix}$ . In Fig. A6 we find that the simulations are less converged as the filament is oriented more end-on to the shock.

To conclude, it seems that the time evolution of  $m_{core}$  and  $\langle v_{x,cloud} \rangle$  are reasonably converged by  $R_{16} - R_{32}$ . However, we caution that other quantities are likely to show greater variation with resolution.

### A3 Convergence Tests

To gain further insight into the effect of the grid resolution on our simulations we examine the variation of some integral quantities computed from the datasets at a particular moment in time. Formal convergence demands that there is an asymptotic levelling off with increasing resolution of a particular quantity.

The variation in  $\langle x \rangle_{cloud}$ ,  $\langle z \rangle_{cloud}$ ,  $\langle v_{x,cloud} \rangle$ ,  $\langle x \rangle_{core}$ ,  $\langle z \rangle_{core}$  and  $m_{core}$  with the spatial resolution for simulation *m10c2l8s* is shown in Fig. A7. It is clear that  $\langle x \rangle_{cloud}$  and  $\langle x \rangle_{core}$  are not yet showing signs of convergence. However,  $\langle v_{x,cloud} \rangle$  and  $m_{core}$  show perhaps the early signs of convergence between  $R_8$  and  $R_{32}$  (the simulation at  $R_4$  is clearly completely unresolved and is ignored).

Figs. A8 and A9 examine the convergence properties for simulations *m10c2l8o60* and *m10c2l8o85*. Broadly similar behaviour is seen. We conclude that our simulations are

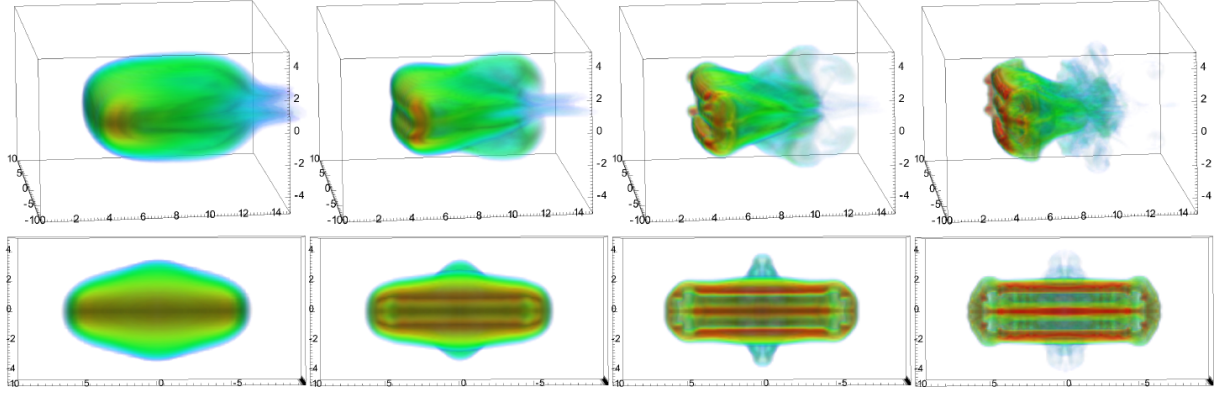


**Figure A1.** The effect of the grid resolution on simulation *m10c2l8s* at  $t = 1.58 t_{cs}$ . From left to right the resolution is  $R_4$ ,  $R_8$ ,  $R_{16}$  and  $R_{32}$ . Side-views are shown in the top row and face-on views in the bottom row.

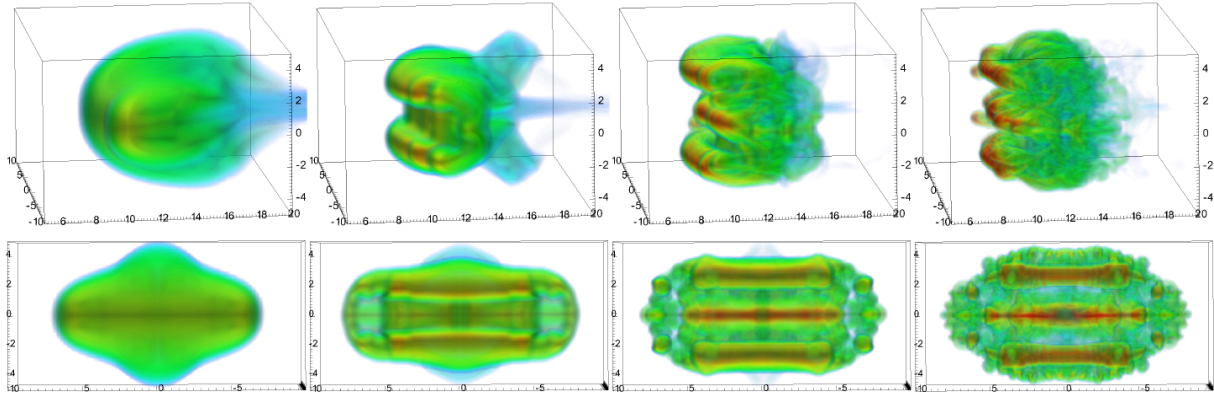


**Figure A2.** As Fig. A1 but at  $t = 2.28 t_{cs}$ .

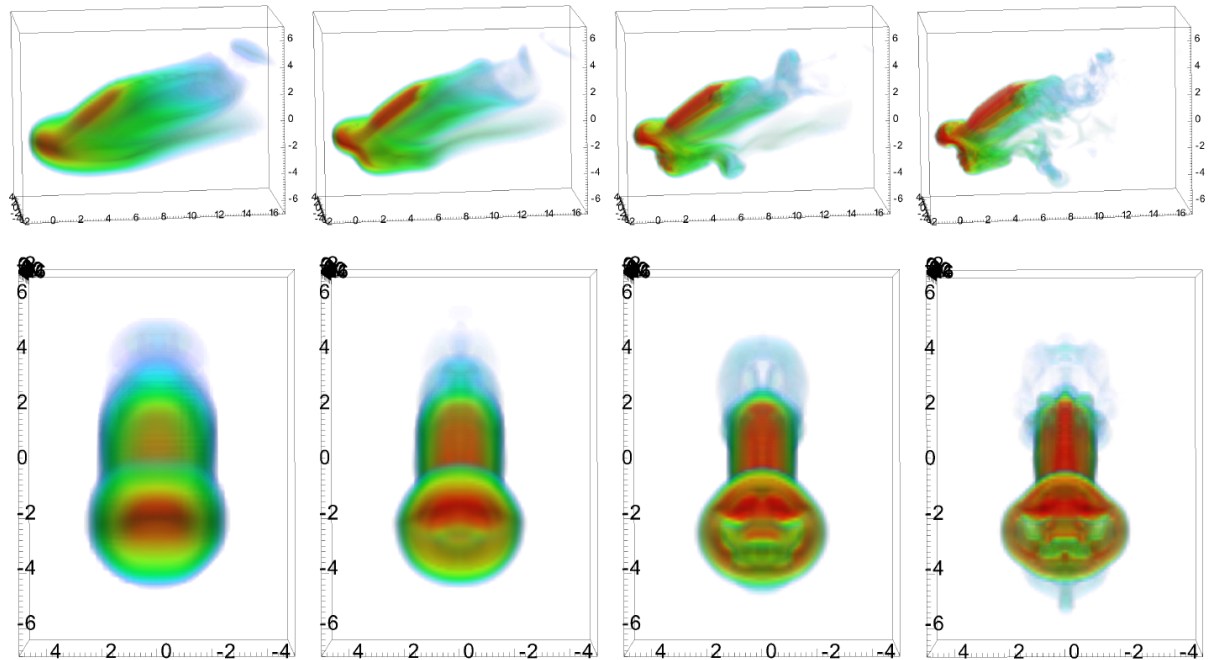


**Figure A3.** The effect of the grid resolution on simulation *m10c2l8o60* at  $t = 1.58 t_{cs}$ . From left to right the resolution is  $R_4$ ,  $R_8$ ,  $R_{16}$  and  $R_{32}$ . Side-views are shown in the top row and face-on views in the bottom row.

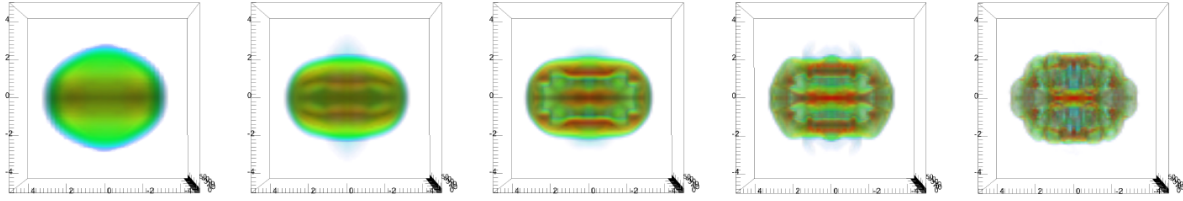


**Figure A4.** The effect of the grid resolution on simulation *m10c2l2s* at  $t = 2.26 t_{\text{cs}}$ . From left to right the resolution is  $R_4$ ,  $R_8$ ,  $R_{16}$ ,  $R_{32}$  and  $R_{64}$ .

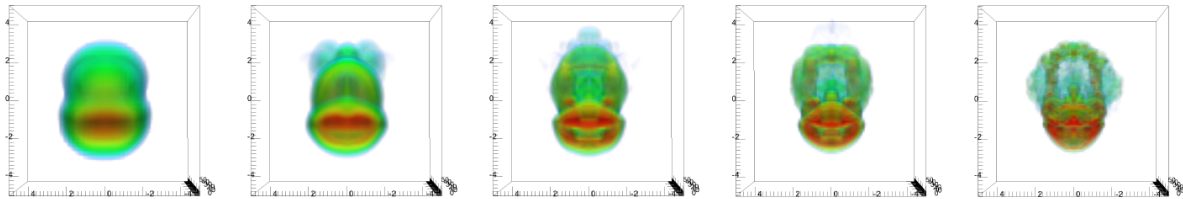


**Figure A5.** The effect of the grid resolution on simulation *m10c2l2o30* at  $t = 2.26 t_{\text{cs}}$ . From left to right the resolution is  $R_4$ ,  $R_8$ ,  $R_{16}$ ,  $R_{32}$  and  $R_{64}$ .

not formally converged, but that the highest resolution simulations have sufficient resolution that some of the integral quantities are showing signs of convergence at  $t = 3.0 t_{\text{cs}}$ . Higher resolution simulations remain desirable to investigate this further.

#### A4 Timescales

Figs. A10 and A11 examine the resolution dependence of  $t_{\text{drag}}$  and  $t_{\text{mix}}$ . In general,  $t_{\text{drag}}$  is broadly stable with resolution. However,  $t_{\text{mix}}$  appears to decrease with increasing resolution, which is different to the behaviour for spherical clouds. For simulation *m10c2l2s* we see convergence towards an asymptote, for  $t_{\text{mix}}$ . So this simulation appears to be formally converged for this particular quantity. However, we do not see such behaviour for the other simulations, so formally they are non-convergent. Having said this, most of them show some signs of levelling off in  $t_{\text{drag}}$  and  $t_{\text{mix}}$ , indicating that their values may be reasonably close to the “true” value. In comparison, we note that at resolution  $R_{32}$  values of  $t_{\text{drag}}$  and  $t_{\text{mix}}$  are on average within a few percent of their values at higher resolutions in simulations of shocks striking spherical clouds (Pittard & Parkin 2016). We might expect this to be true for shock-filament interactions also, but in order to check for false convergence higher resolution simulations are needed.

This paper has been typeset from a  $\text{\LaTeX}$  file prepared by the author.

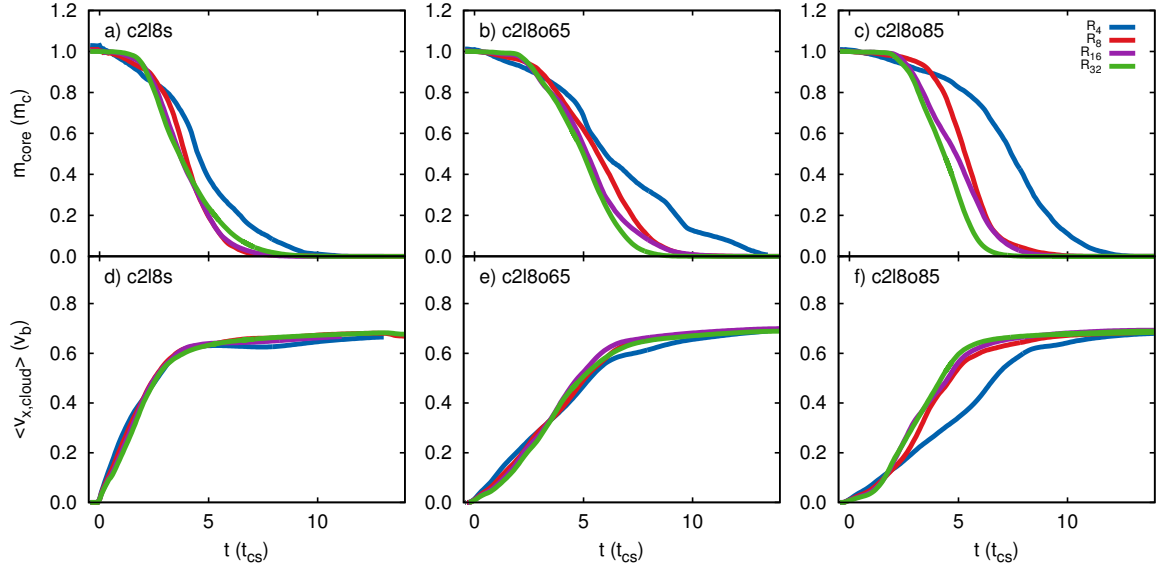


**Figure A6.** Time evolution of the core mass,  $m_{\text{core}}$ , and the mean filament speed,  $\langle v_{x,\text{cloud}} \rangle$ , for simulations (a)  $m10c2l8s$ , (b)  $m10c2l8o65$  and (c)  $m10c2l8o85$ .

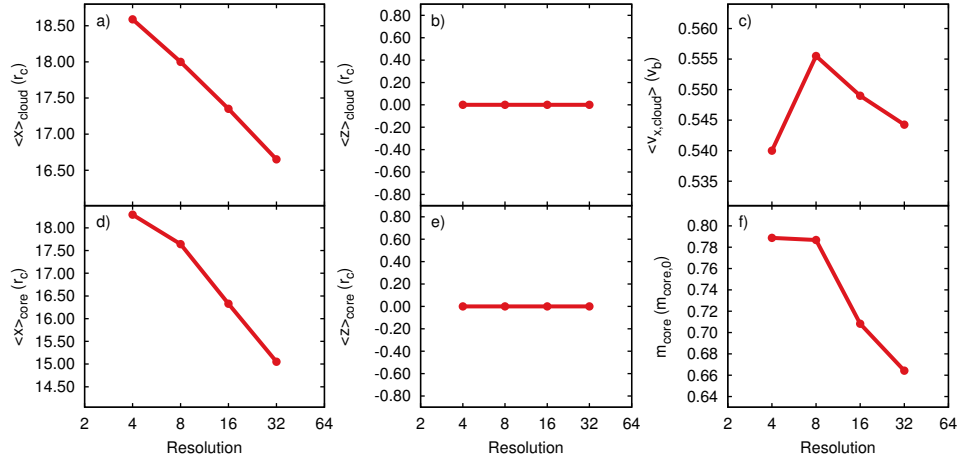


**Figure A7.** Integral quantities from simulation  $m10c2l8s$  at  $t = 3.0 t_{\text{cs}}$ , plotted as a function of the grid resolution.

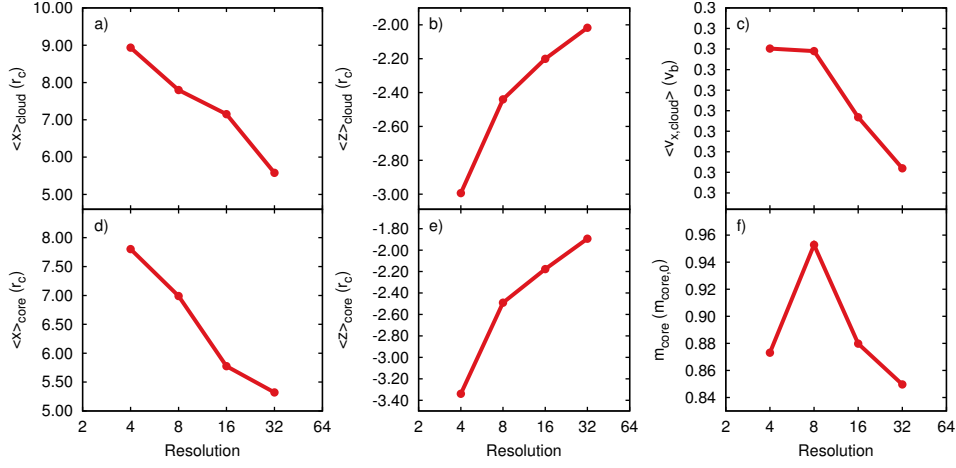


**Figure A8.** As Fig. A7 but for simulation *m10c2l8o60*.

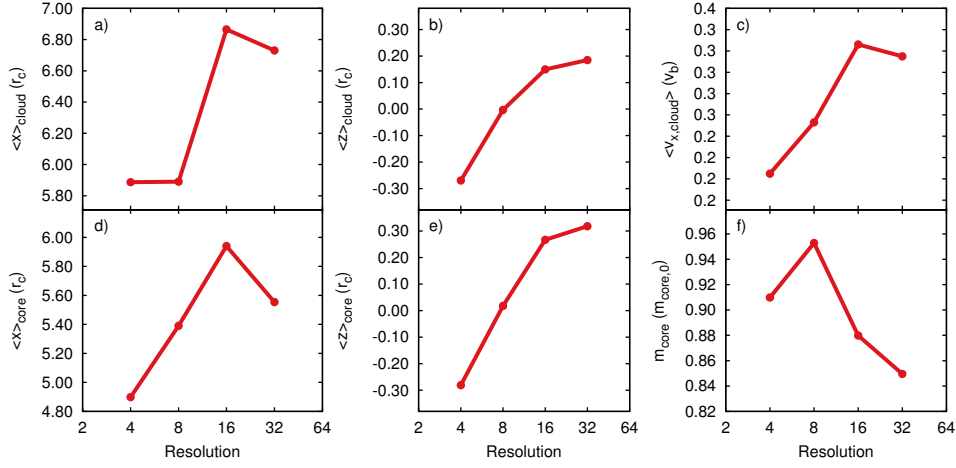


**Figure A9.** As Fig. A7 but for simulation *m10c2l8o85*.

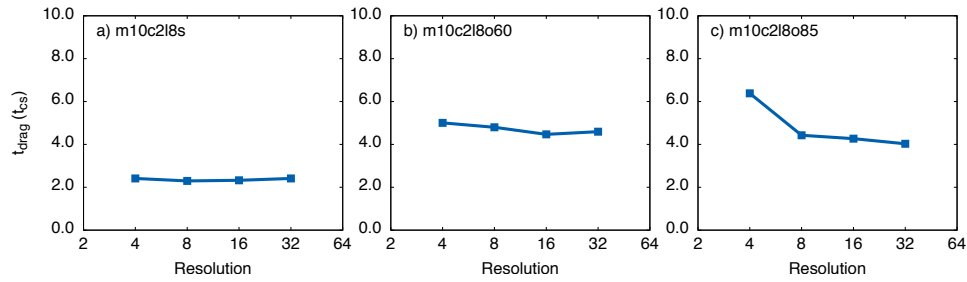


**Figure A10.** Resolution dependence of  $t_{\text{drag}}$  (for the cloud) for simulations a) *m10c2l8s*; b) *m10c2l8o60*; c) *m10c2l8o85*.



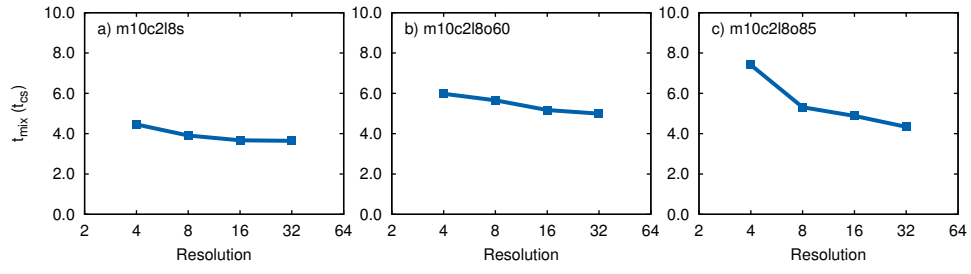


**Figure A11.** Resolution dependence of  $t_{\text{mix}}$  (for the cloud) for simulations a)  $m10c2l8s$ ; b)  $m10c2l8o60$ ; c)  $m10c2l8o85$ .